Journal of Structural Geology 93 (2016) 131–148

Contents lists available at ScienceDirect

Journal of Structural Geology

journal homepage: www.elsevier.com/locate/jsg

Main Frontal thrust deformation and topographic growth of the Mohand Range, northwest Himalaya

Vinee Srivastava [a], Malay Mukul [a, *], Jason B. Barnes [b]

[a] Continental Deformation Laboratory, Department of Earth Sciences, Indian Institute of Technology-Bombay, Powai, Mumbai 400076, India
[b] Landscape Analytics LLC, Seattle, WA 98115, USA

ARTICLE INFO

Article history:
Received 31 December 2015
Received in revised form
24 October 2016
Accepted 26 October 2016
Available online 27 October 2016

Keywords:
Himalayan Main Frontal thrust
Fault propagation folding
Fault damage zone
Frontal fold topography
Real Time Kinematic GNSS
Boundary Element Method
Dislocation modelling

ABSTRACT

The Main Frontal thrust (MFT) uplifts the Himalayan topographic front. Deciphering MFT deformation kinematics is crucial for understanding how the orogen accommodates continuing continental collision and assessing associated hazards. Here, we (a) detail newly discovered fault-zone exposures along the MFT at the Mohand Range front in northwestern India and (b) apply contemporary fault zone theory to show that the MFT is an emergent fault with a well-developed fault zone overlain by uplifted Quaternary gravels over a horizontal length of ~700 m. Northward from the front, the fault zone grades from a central, gouge-dominated core to a hanging-wall, rock-dominated damage zone. We observed incohesive, non-foliated breccia, fault gouge, and brittle deformation microstructures within the fractured country rocks (Middle Siwaliks) and outcrop scale, non-plunging folds in the proximal hanging wall. We interpret these observations to suggest that (1) elastico-frictional (brittle) deformation processes operated in the fault zone at near surface (~1–5 km depth) conditions and (2) the folds formed first at the propagating MFT fault tip, then were subsequently dismembered by the fault itself. Thus, we interpret the Mohand Range as a fault-propagation fold driven by an emergent MFT in contrast to the consensus view that it is a fault-bend fold. A fault-propagation fold model is more consistent with these new observations, the modern range-scale topography, and existing erosion estimates. To further evaluate our proposed structural model, we used a Boundary Element Method-based dislocation model to simulate topographic growth from excess slip at a propagating fault tip. Results show that the frontal topography could have evolved by slip along a (a) near-surface fault plane consistent with the present-day MFT location, or (b) blind MFT at ~3 km depth farther north near the drainage divide. Comparing modelled vs. measured high resolution (~16 cm) topographic profiles for each case provides permissible end-member scenarios of an either dynamically-evolving, high erosion, northward-migrating frontal scarp or a static, low, and symmetric, MHT-related fold, respectively. Our integrated approach is expected to deliver an improved understanding of coupled fault-generated deformation and topographic growth that may be applied more broadly across the entire Himalayan front.

1. Introduction

The India-Eurasia plate margin is one of the world's most active collision zones. It has created the Himalayan mountains for the last ~65 Ma (e.g. Molnar and Tapponnier, 1975; Hodges, 2000; Yin, 2006). The Main Frontal thrust (MFT) defines the orogen's southernmost margin across an entire ~2500 km-long arc between two syntaxes (Schelling and Arita, 1991; Srivastava and Mitra, 1994; DeCelles et al., 1998). The MFT generates and maintains the active, modern Himalayan deformation and topographic front (Nakata, 1989; Yeats and Lillie, 1991; Valdiya, 1992; Wesnousky et al., 1999; Lave and Avouac, 2000; Mukul et al., 2007; Kumar et al., 2010; Burgess et al., 2012) and is thought to be the near-surface expression of the main basal decollément called the Main Himalayan thrust (MHT) (Zhao et al., 1993; Lavé and Avouac, 2000; Bilham et al., 2001). Thus, the MFT-MHT deformation boundary is the contemporary plate interface between India and Eurasia (Bilham et al., 2001; Yeats and Thakur, 2008; Thakur, 2013). Continuing Indo-Asian collision causes strain accumulation along this boundary that is periodically released during great ($M > 8$) earthquakes (Bilham et al., 2001). It is postulated that the MFT is

* Corresponding author.
E-mail address: malaymukul@iitb.ac.in (M. Mukul).

http://dx.doi.org/10.1016/j.jsg.2016.10.009
0191-8141/

fully locked along its frontal, 100 km across-strike width over its entire strike-parallel length (Stevens and Avouac, 2015). During great earthquakes, the MFT can unlock and transfer strain along the MHT to the MFT (Lavé and Avouac, 2000). Over centuries, MFT motion has caused frequent, large earthquakes that demonstrate how vital the MFT-MHT deformation zone is for Himalayan tectonics, seismicity, and the associated natural hazards (Powers et al., 1998; Wesnousky et al., 1999; Kumar et al., 2001, 2006, 2010; Malik and Nakata, 2003; Lave et al., 2005; Malik et al., 2010; Burgess et al., 2012; Sapkota et al., 2013). Large magnitude slip events and earthquakes remain a principal hazard because the Himalayan orogenic wedge thrust belt continues to cycle through various deformation states in an attempt to maintain equilibrium in response to plate motion stresses (e.g. DeCelles and Mitra, 1995; Mukul et al., 2007).

Existing MFT fault zone deformation studies have been restricted to trench excavations that typically access a small fraction of the fault zone or only minor splays off of it (Kumar et al., 2001, 2006, 2010; Malik and Nakata, 2003; Lave et al., 2005; Malik et al., 2010; Mugnier et al., 2013; Sapkota et al., 2013; Vassallo et al., 2015). Although these studies provide important insights for paleo-earthquake behavior, they are of limited use for understanding how the geometry and kinematics of the MFT has evolved throughout the Quaternary. Fortunately, a complimentary framework exists to describe and understand major fault zones that can address this deficiency. In general, major fault zones are meters to kilometers in thickness and characterized by different components with distinctive geometries and textures (e.g. Shipton and Cowie, 2003; Gudmundsson, 2011). They commonly contain a highly deformed core (or slip zone) with maximum grain-size reduction that is flanked on both sides by damage zones in which deformation decreases and grain size increases outward until reaching intact rock that remains unaffected (Fig. 1) (Flinn, 1977; Aydin, 1978; Scholz, 1987; Evans, 1990; Cowie and Scholz, 1992; Chester et al., 1993; Newman and Mitra, 1993; Caine et al., 1996; Sibson, 2003; Wibberley and Shimamoto, 2003; Kim et al., 2004; Shipton et al., 2006; Mitchell and Faulkner, 2009; Gudmundsson, 2011). Fault damage zone rocks are classified by their matrix content, grain size, cohesion, and degree of foliation (Sibson, 1977; Marshak and Mitra, 1988; Shipton and Cowie, 2003). Development of different structures within these damage zones provide valuable information about fault development (Perry, 1978; Aydin, 1988; McGrath and Davison, 1995; Vermilye and Scholz, 1998, 1999; Kim et al., 2001a, b; Nicol et al., 2002), associated fluid flow (Sibson, 1996; Martel and Boger, 1998), and even earthquake initiation and termination (Sibson, 1985; King, 1986; Aki, 1989; Thatcher and Bonilla, 1989; Kim et al., 2004). Furthermore, the physical dimensions of a fault zone are important because they scale and vary along strike with displacement (e.g. Torabi and Berg, 2011) and hence provide additional insight into fault growth (Walsh and Watterson, 1988; Peacock and Sanderson, 1991; Cowie and Scholz, 1992; Gudmundsson, 1992; Cartwright et al., 1995; Dawers and Anders, 1995; Cladouhos and Marrett, 1996; Walsh et al., 2002; Kim and Sanderson, 2005; Soliva and Schultz, 2008) and the topographic response to it (Allen et al., 2013; Ellis and Barnes, 2015). To date, the MFT has not been studied within this conceptual framework, perhaps in part, because it remains difficult to observe at the surface as a commonly documented blind fault (Stein and Yeats, 1989; Valdiya, 1992; Yeats et al., 1992).

Quaternary MFT motion has produced range-scale topography and folding (e.g. Karunakaran and Ranga Rao, 1979; Raiverman et al., 1994; Powers et al., 1998; Wesnousky et al., 1999; Lave and Auovac, 2000; Lave et al., 2005; Delcaillau et al., 2006; Malik et al., 2010; Burgess et al., 2012; Thakur, 2013). Unfortunately, a wide range of structural models have been proposed to explain the

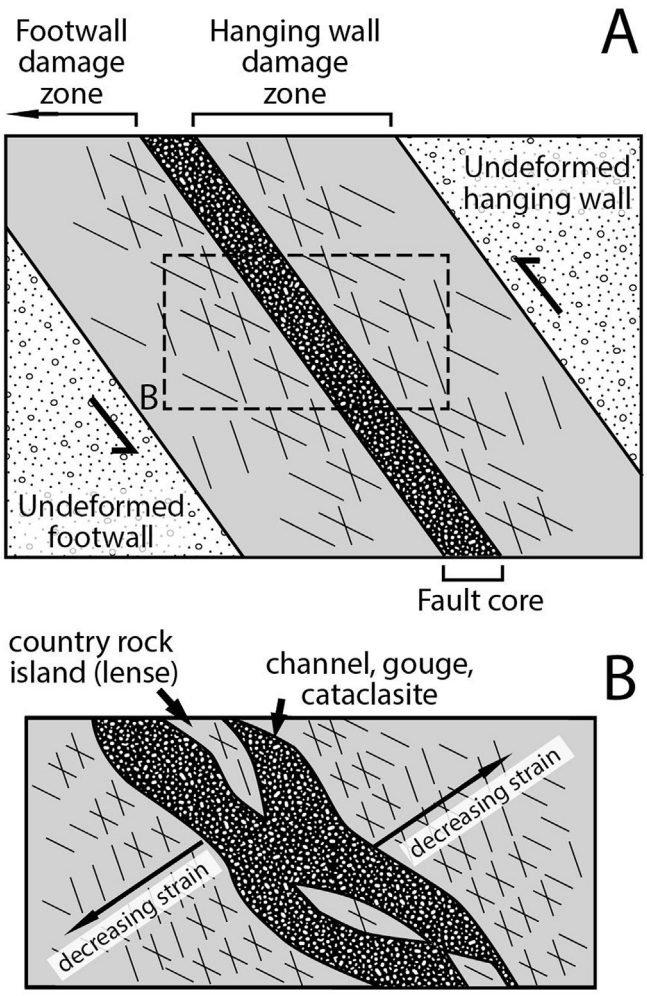

Fig. 1. Schematic thrust fault damage zone in a sedimentary country rock (modified from Shipton and Cowie, 2003; Mitchell and Faulkner, 2009; Gudmundsson et al., 2010). (A) Note the major components: core, damage zone (in the footwall, hanging wall), and the adjacent undeformed country rock. (B) In detail, the fault zone contains a core with channels surrounding islands of more intact, deformed country rock that transition into damage zones characterized by decreasing strain with distance from the core.

evolution of the MFT and its associated folds because the fault has not been observed at the surface in any of these studies. For example, the MFT is described as blind (Mukhopadhyay and Mishra, 2004), emergent (Raiverman et al., 1994; Powers et al., 1998), blind, but very close to the surface and recognizable in seismic sections and boreholes (Wesnousky et al., 1999; Mishra and Mukhopadhyay, 2002), or simply a zone of intense brittle deformation (Srivastava and John, 1999). These discrepancies lead to nontrivial differences in shortening estimates within the MFT thrust sheet; in the Mohand Range, for example, a blind MFT model estimated ~17% shortening (Mishra and Mukhopadhyay, 2002) compared to an emergent MFT model that estimated ~27% shortening (Powers et al., 1998). Furthermore, such disparities have led to a plethora of interpretations for the associated fold kinematics such as fault-propagation folding (e.g. Lave et al., 2005), fault-bend folding (e.g. Wesnousky et al., 1999; Mishra and Mukhopadhyay, 2002), or just a generic growing anticline (e.g. Powers et al., 1998; Burgess et al., 2012). In some cases, including at Mohand, even the exact same anticline has been interpreted differently (e.g. compare Fig. 2C and D) (cf. Raiverman et al., 1994; Powers et al.,

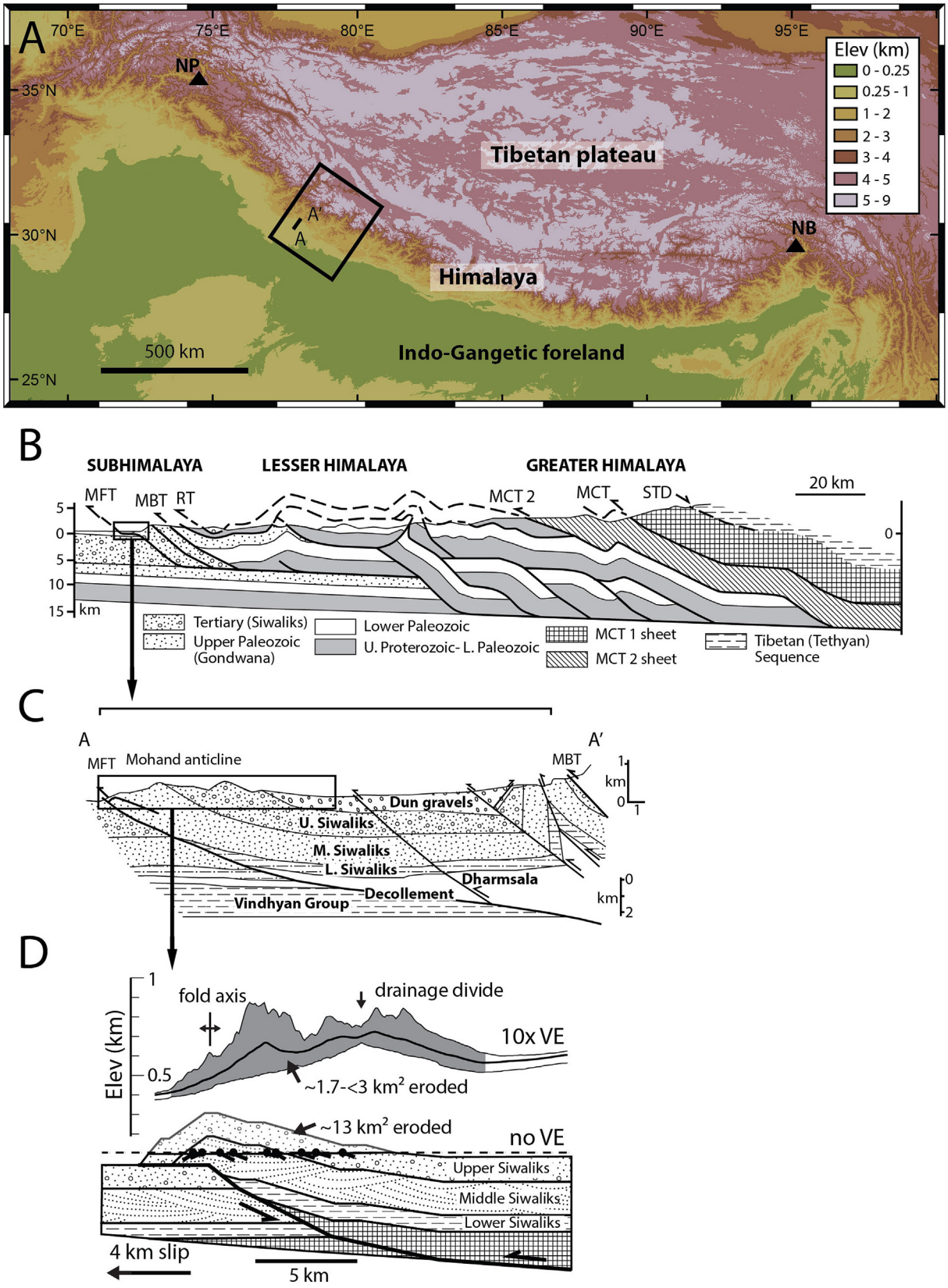

Fig. 2. The Himalayan fold-thrust belt. (A) Topography (90 m SRTM v4.1 DEM) with salient and recess morphology observed at 100-km scales along the range front. Syntaxes: NP = Nanga Parbat; NB = Namche Barwa. (B) Representative Kumaon-Garhwal regional cross section for boxed area in part A (simplified from Srivastava and Mitra, 1994; Mitra et al., 2010). MFT = Main Frontal thrust, MBT = Main Boundary thrust, RT = Ramgarh thrust, MCT = Main Central thrust, MCT 2 = Munsiari thrust, STD = South Tibetan Detachment. (C) Cross section across the Dun valley near Dehra Dun emphasizing the Mohand anticline structure (after Thakur and Pandey, 2004). Note the near surface vertical scale is exaggerated. Location is A-A′ in part A. (D) Swath elevation profile above the Mohand anticline balanced section of Mukhopadhyay and Mishra (2004) and estimated rock area erosion from above the present-day topographic surface (location in Fig. 3; modified from Barnes et al., 2011).

1998; Mishra and Mukhopadhyay, 2002).

All proposed models for the Mohand Range involve extrapolation of geologic structures above and below the present-day erosion surface. Extrapolation to depth has largely depended on 30-yr old Oil and Natural Gas Corporation (ONGC) seismic reflection profiles and two exploratory wells whose lithologs are not in the public domain (Raiverman et al., 1994). For some time now it has been acknowledged that the available information is variably sourced and appears to exhibit considerable inconsistency (Mishra and Mukhopadhyay, 2002). Without surface expression of the MFT, extrapolation can be based on entirely different conceptual models (e.g. Raiverman et al., 1994; Powers et al., 1998; Mishra and Mukhopadhyay, 2002) that cannot be properly validated by field data, thus derived cross sections possess uncertain admissibility (Elliott, 1983). In summary, lack of direct observations of the MFT continues to inhibit (1) our understanding of its geometry, kinematics, and evolution, and as a result, (2) further elucidation of its vital role as an active, hazardous, collisional plate interface that continues to facilitate southward propagation of the largest orogen by range-front folding and uplift.

The purpose of this paper is to document several newly discovered, exposed sections of the MFT fault zone at the northwest Himalayan front near Mohand. We place our observations within the contemporary fault-core and damage zone framework outlined above. We also provide new high resolution, field-based topographic data for further constraining existing structural models of MFT development. We then examine the admissibility of these models using the field data to constrain the geometric and kinematic boundary conditions to resolve a preferred structural model for the MFT and Mohand Range. Next, we use a numerical model, constrained by boundary conditions specified by the most admissible structural model, to explore the co-evolution between MFT deformation and topographic growth across the central Mohand Range. This integrated approach (combining contemporary fault zone theory, tectonomorphic field data, and dislocation modelling) is expected to provide a novel blueprint for improved understanding of coupled fault zone deformation and topographic growth in elastico-frictional settings across the entire Himalayan front with implications for active, collisional wedge development worldwide.

2. Geologic setting

The Himalaya form an arc between two syntaxes in map view (Fig. 2A) (Macedo and Marshak, 1999; Bendick and Bilham, 2001). In transport-parallel cross section, the Himalayan thrust belt is bounded by the basal Main Himalayan thrust (MHT) at depth (Fig. 2B) (e.g. Schelling and Arita, 1991; Nelson et al., 1996) and also contains E-W striking listric thrust faults that sole into it. The major listric thrust faults have developed from hinterland to foreland (north to south) as follows: Main Central thrust (MCT), Main Boundary thrust (MBT), Ramgarh thrust (RT), and the Main Frontal thrust (MFT) (see reviews in Hodges, 2000; Yin, 2006). The MFT is the most southern of these faults (Le Fort, 1975; Nakata, 1989; Thakur, 2013) and soles into the MHT at depth (Srivastava and Mitra, 1994; DeCelles et al., 1998). In this study, we focus on the near-surface portion of the MFT and its proximal hanging wall structures and topography (Fig. 2B–D).

The MFT is the largest active structure in the Himalayan orogen (Gansser, 1964; Nakata, 1989; Yeats et al., 1992; Bilham et al., 1998; Lavé and Avouac, 2000; Avouac, 2003; Yin, 2006; Yeats and Thakur, 2008), although more minor blind thrust faults have also been postulated farther south (Thakur et al., 2007; Yeats and Thakur, 2008). The MFT has been called the Himalayan Frontal Boundary (HFB), Himalayan Frontal Fault (HFF), Himalayan Frontal thrust (HFT), and Foothill thrust (Nakata, 1972; Valdiya, 1992; Thakur, 2013). It is variably expressed as an emergent, near surface or blind thrust fault that places older Siwaliks sedimentary rocks over younger Indo-Gangetic alluvium (Gansser, 1964, 1981; Yeats and Lillie, 1991). Where blind, the MFT is inferred from the emergent, Himalayan topographic front (Karunakaran and Ranga Rao, 1979; Yeats and Lillie, 1991; Valdiya, 1992).

2.1. The Main Frontal Thrust (MFT) and Mohand Range

In the Garhwal Himalaya (northwest India), the MFT and related structures have been the focus of significant research since the 1960s (e.g. Sahni and Khan, 1963; Rao, 1993; Mukhopadhyay and Mishra, 2004; Barnes et al., 2011; Kirby and Whipple, 2012; Allen et al., 2013; Mishra and Chakrapani, 2014). In the Dehra Dun area, the ~80 km-long Mohand Range defines the frontal topography and is a MFT-related, NW-SE trending ridge bounded by the Yamuna and Ganga rivers to the northwest and southeast, respectively (Fig. 3) (Rao et al., 1974). In the Mohand Range, the MFT places Middle Siwaliks rocks over Quaternary Doon gravels and is locally called the Mohand thrust (Karunakaran and Ranga Rao, 1979). Here, the MFT and Mohand Range is commonly depicted as a blind thrust (Raiverman et al., 1990) within a fault-bend fold (e.g. Fig. 2D) (Mishra and Mukhopadhyay, 2002; Mukhopadhyay and Mishra, 2004). However, previous cross sections displayed the MFT as a 2-km-wide zone of intense brittle deformation (Srivastava and John, 1999) or as an emergent fault (Powers et al., 1998; Wesnousky et al., 1999; Thakur, 2004).

Deformation along the MFT in the Mohand Range post-dates the Upper Siwalik section and is postulated to initiate after ~0.78 Ma. This age corresponds to the Brunhes-Matuyama boundary recorded in the Boulder conglomerates or the youngest Upper Siwalik unit (Sangode et al., 1996, 1999; Kumar et al., 2003a, 2003b). A 0.0037 ± 0.00022 Ma charcoal-based radiocarbon date from an uplifted fluvial terrace in the Shahjahanpur area (between 2 & 3 in Fig. 3) indicates that the MFT motion is > ~0.0035 Ma (Wesnousky et al., 1999). Therefore, MFT motion here is between ~0.78 and 0.0035 Ma. Dates from the top of the Upper Siwaliks conglomerate nearby are 0.5 to 0.2 Ma (Rao, 1993; Sangode et al., 1996, 1999) and the oldest overlying gravels are 0.004 Ma (Singh et al., 2001), further constraining the timing of deformation (Thakur, 2013). Barnes et al. (2011) used a typical fault displacement-tip propagation ratio to estimate the age of the Mohand Range at 0.22–0.47 Ma. Local deformation rates are ~7 mm/yr of vertical uplift (Kumar et al., 2006), ~12 mm/yr shortening, and ~14 mm/yr of slip (Powers et al., 1998; Wesnousky et al., 1999), with shortening rates at 11–14 mm/yr (Thakur et al., 2014) and a long-term velocity of 18.5 ± 1.8 mm/yr in the northwest Himalayan region (Stevens and Avouac, 2015). However, regional Global Positioning System (GPS) measurements from 1995 to 2008 indicate that the MFT is locked with no contemporary slip along it (Jade et al., 2014) that is supported by an interseismic coupling model of the MHT (Stevens and Avouac, 2015).

3. Methods

This work was motivated by the discovery of multiple exposures of an emergent MFT fault zone along the southern Mohand Range front. We collected detailed structural, stratigraphic, lithologic, and grain-size data throughout the MFT fault zone core and damage zone along 4 strike-perpendicular traverses (1–4 in Fig. 3). We also collected 3 oriented, Middle Siwalik sandstone samples; 2 from within the fault damage zone and 1 from outside it for comparison (a-c in Fig. 3). We used these samples to create regional transport-parallel (NE-SW), oriented thin sections for microstructural

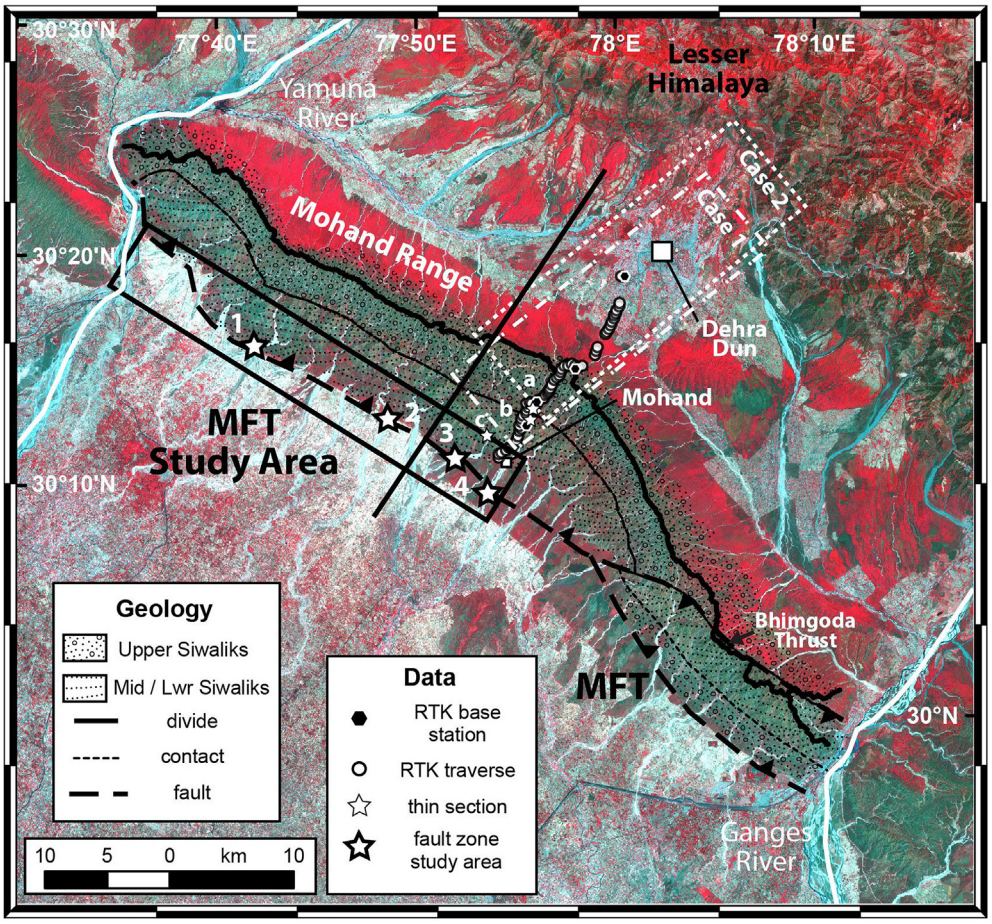

Fig. 3. Landsat TM image of the Mohand Range and Main Frontal thrust (MFT) study area. Stars are the MFT fault zone exposure traverses; 1- Barkala; 2- Kaluwala; 3- Khajnawar, and 4- Mohand Rao. Straight black line is the location of Fig. 2D. Dots are the Real Time Kinematic Global Navigation Satellite System traverse locations used to quantify a SW-NE elevation profile for comparison with dislocation model projections for two different cases.

analysis, including grain-scale sizes and patterns, in order to determine the deformation mechanism(s) that operated within the fault zone (Sibson, 1977; Blenkinsop, 2000; Passchier and Trouw, 2005). We also conducted field-based measurements of the Mohand Range topography to develop a high-resolution representation of the surface response to MFT motion. We used Real Time Kinematic Global Navigation Satellite System (RTKGNSS) technology that included both a stationary base (also called reference receiver) and a roving receiver in differential mode (e.g. Bernhard et al., 2008; Gleason and Gebre-Egziabher, 2009). We used four base stations (black symbols in Fig. 3) that calculated position error by comparing measured and known positions and transmitted the error to the remote roving receiver in real time. The remote receiver then corrected its calculated position using this transmitted error. Our survey achieved a horizontal and vertical position uncertainty of ~16 cm. We moved the RTKGNSS rover along a central transect of the range surface in December 2013 to obtain a representative elevation profile across the range (dots in Fig. 3) (e. g. Bangen et al., 2014; Sinha et al., 2014).

We employed forward modelling to understand the integrated evolution of MFT slip, topographic growth, and erosion along the central Mohand Range where the fault zone has the maximum thickness exposed (extent of both cases in Fig. 3). Major faults rupture in segments that coalesce resulting in lateral and frontal propagation of the fault-tip so that the fault damage zone width also increases with displacement (e.g. Fig. 8 in Shipton and Cowie, 2003). This fault growth process results in an integrated displacement field that is highest near the fault center and zero at the tip (Cowie and Shipton, 1998; Shipton and Cowie, 2003) via the initiation, propagation, and interaction of slip along individual fault traces (e.g. Cowie and Scholz, 1992; McGrath and Davison, 1995). Because the integrated displacement field is coupled with topographic growth for dip-slip faults (Densmore et al., 2007; Ellis and Barnes, 2015), the MFT and proximal hanging wall can be simulated as a single elastic dislocation (or crack) in an elastico-frictional deformation regime (Gudmundsson, 2011). We further assume that the topography in the Mohand Range was built over multiple large coseismic events during which slip was transferred from the hinterland to the MFT as the Himalayan front is locked during the interseismic period near the surface trace of the MCT (e.g. Stevens and Auovac, 2015), and the post seismic relaxation is typically down-dip of the coseismic rupture. As we cannot identify individual coseismic events, we used a “cumulative” slip dislocation plane that represents the sum total of coseismic events (minus the post-seismic down-dip events) that would best simulate the observed topography. In this study, we used the Okada (1985)-dislocation model based on a Boundary Element Method formulation (Crouch and Starfield, 1983; Toda et al., 2005) (Appendix A). Inputs include estimates of dislocation strike, strike-parallel length, strike-perpendicular width, dip angle, dip direction, cumulative slip along the simulated fault plane, and coordinates of the dislocation trace (fault plane) if emergent, or its surface projection if

Table 1
Fault parameters used for dislocation modelling.

MFT	Fault slip[a] (m)	Fault dip (°NE)	Strike (°)	Top depth[b] (km)	Fault width (strike perpendicular) (km)	Fault length (strike parallel) (km)
Case 1	900 ± 5	30 ± 1	320	0.2 ± 0.1	30 ± 5	8 ± 0.1
Case 2	815 ± 5	30 ± 1	320	3 ± 0.05	31 ± 1	9 ± 0.5

[a] Cumulative slip.
[b] Fault depth in up-dip direction at front.

blind (Table 1). We used a strike of 320° and dip of 30°NE based on drill hole and seismic reflection data for the MFT (Wesnousky et al., 1999 and references therein; Thakur, 2013). In detail, the 30° dip is well-constrained by deep borehole data, a shallow exploratory well, and seismic reflection lines in southern Mohand as well as trench data that exposes contact between the Middle Siwaliks and the alluvial plains along the HFT at a 30°NE dip angle (Thakur, 2004). We simulated a strike-parallel dislocation length of ~8–9 km that is approximately the segment length of the MFT that has produced maximum fault zone deformation, best developed a fault core and damage zone, as well as includes the area we obtained topography data for results evaluation (Fig. 3). We systematically varied the other parameters to obtain a modelled profile closest to the measured cross-sectional profile (Appendix B; Table 1). For blind dislocation models, depths of its top and bottom tip-lines must be defined. However, as the MFT is the surface equivalent of the MHT or soles into it, we avoided a physically implausible down-slip termination of the dislocation at finite depth. We assumed material deformation to be elastico-frictional with a Poisson's Ratio of 0.25 (sandstones vary from 0.21 to 0.38) and Young's Modulus of 10 GPa (sandstones vary from 10 to 20 GPa) (see Table 6.1 in Fossen, 2010). We chose these representative values for Middle Siwaliks sandstones in near-surface conditions because they occupy most of the central Mohand Range (Fig. 3).

4. Results

Here, we summarize our observations and sample results from four regional transport-parallel transects of the MFT fault zone exposed along ephemeral channels draining the frontal-most portion of the Mohand Range (1–4 in Fig. 3). From northwest to southeast, these traverses are Barkala Rao (1), Kaluwala Rao (2), Khajnawar Rao (3), and the central Mohand Rao (4). In these transects, Siwaliks rocks in the MFT fault zone form strath terraces with the following general stratigraphy from the top downward: 1–3 m thick loamy sand soils, 2–3 m thick pebble-cobble gravels, then underlying Middle Siwaliks sandstones outcropping ~10–15 m above the modern stream bed (Wesnousky et al., 1999). In all locations except the Barkala Rao section, our descriptions only involve the MFT fault zone and its hanging wall because the footwall remains buried.

4.1. Barkala Rao

In the field, Middle Siwaliks rocks (mapped by Karunakaran and Ranga Rao, 1976; Thakur, 1992; Najman et al., 1993) directly overlie Quaternary Doon gravels along an ~10 m-wide MFT fault zone exposure with a core ~15–20 cm in width (1 in Fig. 3; Fig. 4A). Here, the gravels have been uplifted by the MFT (Wesnousky et al., 1999) and the bedding is warped and tilted to the northeast near the fault zone (Fig. 4A). The MFT exposure exhibits a well-developed fault zone with distinct core and damage zones. Breccia and zones of localized gouge formation indicate brittle deformation in the frontal part (Fig. 4B–D). Away from the fault zone, we observed outcrop scale, upright with near vertical axial plane, symmetric antiform-synform fold pairs (Fig. 5A) with uniformly dipping limbs at 45° (axial plane 354°/81°E [Fig. 5B]) and a sub-horizontal enveloping surface along a SW-NE transport parallel traverse in the hanging wall. The relief generated by the outcrop-scale folding and uplifted gravels is ~10–15 m from the modern streambed (Figs. 4A and 5A).

4.2. Kaluwala Rao

The Kaluwala Rao section lies more towards the central Mohand Range (2 in Fig. 3). Here, the MFT is exposed as a well developed, ~250 m-wide fault zone exposure characterized by extreme grain-size reduction that has resulted in incohesive and powdery fault gouge created by MFT motion (Fig. 6A–C). Parts of the fault zone are reddish brown and others are gray (Fig. 6B and C). The gray gouge is derived from the gray Middle Siwalik sandstones and the red gouge is seen at places in irregular contact with the gray gouge (Fig. 6B and C). Topography generated over the fault gouge in the MFT zone is ~5–10 m in elevation (Fig. 6A, C) and possesses gullying from water erosion of the fine-grained material (Fig. 6A–C). The red gouge is probably due to weathering reactions with iron-rich fluid penetration into the fault zone. Although the MFT fault zone is dominated by fine grained, powdered fault gouge, some less-deformed blocks of Middle Siwaliks country rocks have escaped pulverization and occur as islands 1–10 cm in diameter randomly distributed throughout the gouge. We also observed a single, isolated island ~1 m in width within the fault gouge that was intensely fractured (Fig. 6E and F). Although not well preserved, structural data in the frontal part indicated remnants of symmetric folds with axial plane 300°/87°NE that were outcrop scale and upright (Fig. 6G).

4.3. Khajnawar Rao

The frontal topography of the central Mohand Range in the Khajnawar Rao section (3 in Fig. 3) possesses highly deformed, very fine-grained powdery fault gouge (Fig. 7A–C) overlain by uplifted gravel ~10–15 m above the streambed (Fig. 7B). The frontal part of the MFT fault zone exposure is very similar to that observed in the Kaluwala Rao (e.g. Fig. 6A–C). It consists dominantly of gray and reddish brown, fine-grained gouge interspersed with cm-scale islands of Middle Siwaliks rocks (Fig. 7A). Trenches cut into the Khajnawar Rao mouth below the active channel revealed a steep, abrupt boundary between the Siwaliks beds and alluvial, floodplain deposits along a low-angle thrust fault with signatures of repetitive seismic events on the emergent fault that uplifted terrace deposits (Kumar et al., 2006). Farther northeast (~150 m from the front) in the MFT hanging wall, we observed several meter-scale islands of less-deformed Middle Siwalik rocks with preserved south and north-dipping relict bedding (Fig. 8A and B). These islands consist of highly fractured and brecciated Middle Siwaliks rocks (Fig. 8C) that are surrounded by deformed and powdery gouge material as a fine-grained channel (Fig. 8D). We also observed folds within the islands in the fault gouge (Fig. 9A), indicating meter-scale folding in the frontal Mohand Range (Fig. 9B). Farther inboard, gouge-

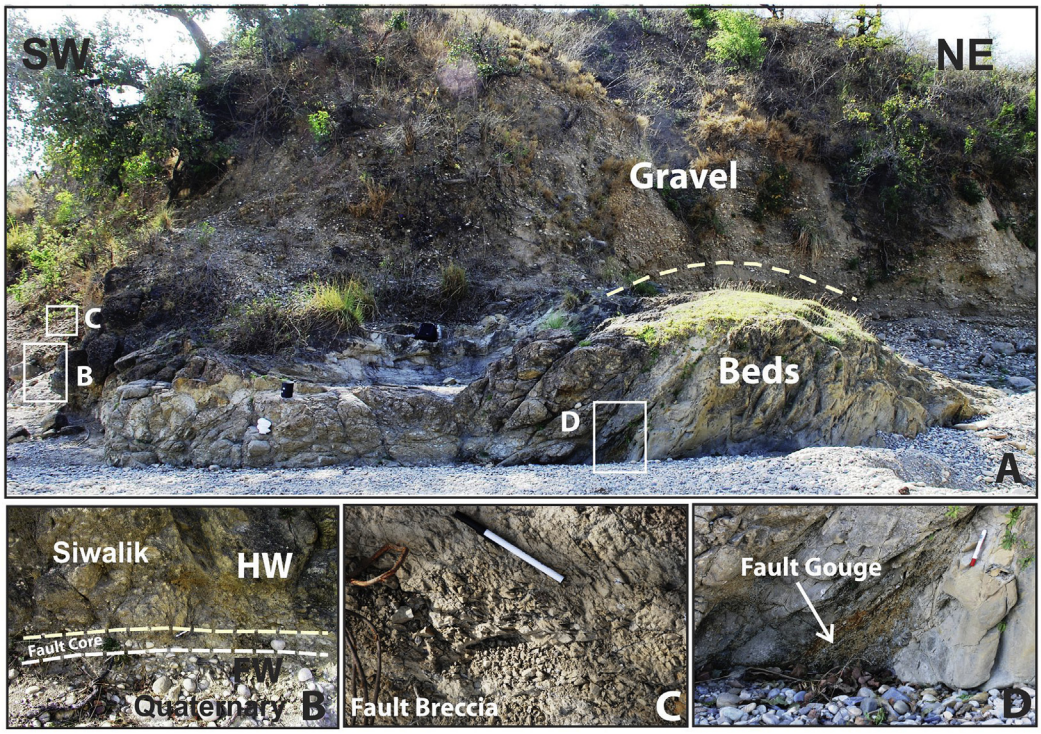

Fig. 4. Westernmost exposure of the Main Frontal thrust fault zone in Barkala Rao (1 in Fig. 3). (A) Frontal topography with exposed Middle Siwalik beds capped by tilted and warped gravels. (B) The fault core (~15–20 cm across) creates contact between the Middle Siwaliks hanging wall (HW) and the Dun gravels foot wall (FW). (C) Fault breccia in the damage zone proximal to the fault core with a standard pen (~15 cm) for scale. (D) The more distal damage zone characterized by fault gouge within fractured Middle Siwaliks rocks with a pen (~15 cm) for scale.

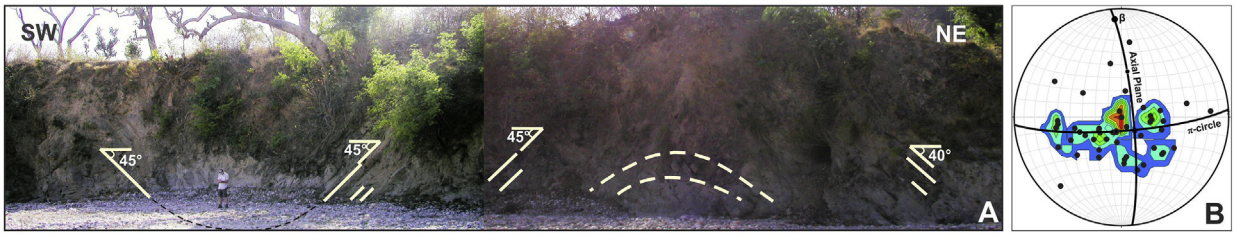

Fig. 5. Proximal hanging wall geometry of the MFT in Barkala Rao (1 in Fig. 3). (A) Outcrop scale, upright, non-plunging, symmetric antiform and synform folds along a NE-SW stream flank exposure. Person is 1.8 m tall. (B) Structural data (52 poles to bedding) from the frontal portion indicating upright, non-plunging folds with near vertical axial plane 354°/81°E and fold axis (β) 10° → 355°. The π-circle is the great circle along which poles to bedding lie.

dominated exposures with interspersed meter-scale islands are gradually replaced by exposures dominated by northeast-dipping Middle Siwaliks sandstones with fine-grained fault gouge deformation bands developed within them (Fig. 9C and D). We also observed fractured, northeast-dipping Middle Siwaliks rocks outside the MFT fault zone starting at ~700 m from the topographic front (Fig. 9D).

4.4. Mohand Rao

The Mohand Rao section lies in the most central part of the Mohand Range where Middle Siwaliks rocks overlie Doon gravels similar to the other fault zone exposures. Here, there is an ~10-15 m-wide fault zone exposure with gravels uplifted ~1–3 m above the present-day channel. These gravels are also present as slope failure-related hill slope debris (Fig. 10A). Interestingly, the wide zone of fault-related gouge we observed in the Kaluwala and Khajnawar sections (2, 3 in Fig. 3) was absent here. However, similar to the Barkala section, we observed outcrop-scale, upright, open, non-plunging antiformal and synformal folds with both northeasterly and southwesterly-dipping limbs along the western channel bank (Fig. 10B and C). The fold limbs dip symmetrically ~30° NE and SW with an axial plane of 288°/88°NE (Fig. 10D).

4.5. Fault zone petrography, deformation microstructures and grain-size analysis

The islands within the fault zone allow us to investigate the microscopic deformation mechanisms and grain-size reduction processes operational within it. First, the Middle Siwaliks sandstone protolith petrography outside the fault zone (a in Fig. 3) is framework quartz, feldspar, lithofragments, muscovite, and biotite minerals in a carbonate-rich matrix (Fig. 11A). We observed undulose extinction in almost all quartz grains and deformation bands, subgrains, and intracrytalline, healed fractures in some of them. Some lithofragments contained elongated quartz grains with strong preferred orientation. Mica flakes showed kinking and undulose extinction. However, these quasi-plastic microstructures

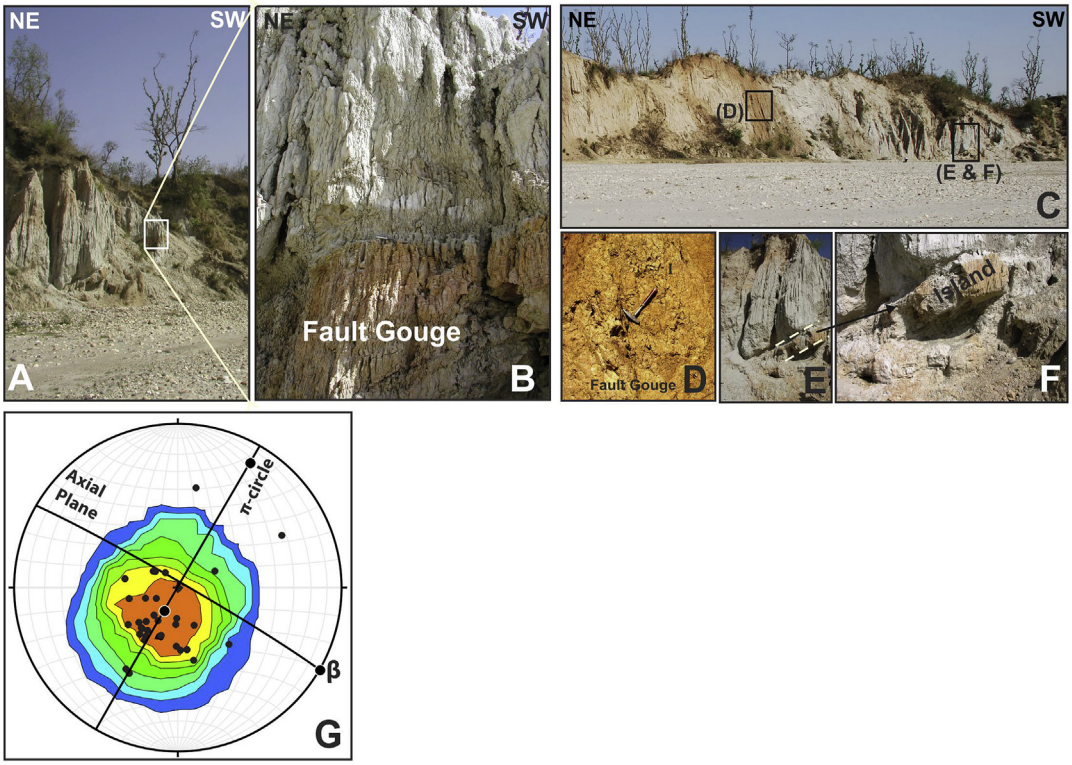

Fig. 6. Deformation structures observed in the MFT fault zone exposed along the Kaluwala Rao (2 in Fig. 3). (A) Overview of the highly pulverized fault gouge material in the fault core exposed in ~10 m high cliff. (B) Irregular contact between dark and light gray fault gouge material with a pen (~15 cms) for scale. (C) View of the exposed ~250 m wide MFT fault zone. (D) Gouge with standard geological hammer (~30 cm) for scale. (E) and (F) single undeformed island within the gouge with standard geological hammer (~30 cm) for scale. (G) Structural data (43 poles to bedding) from the frontal part of the section, indicating upright, non-plunging folds with near vertical axial plane 300°/87°NE and fold axis (β) 0°→120°. The π-circle is the great circle along which poles to bedding lie.

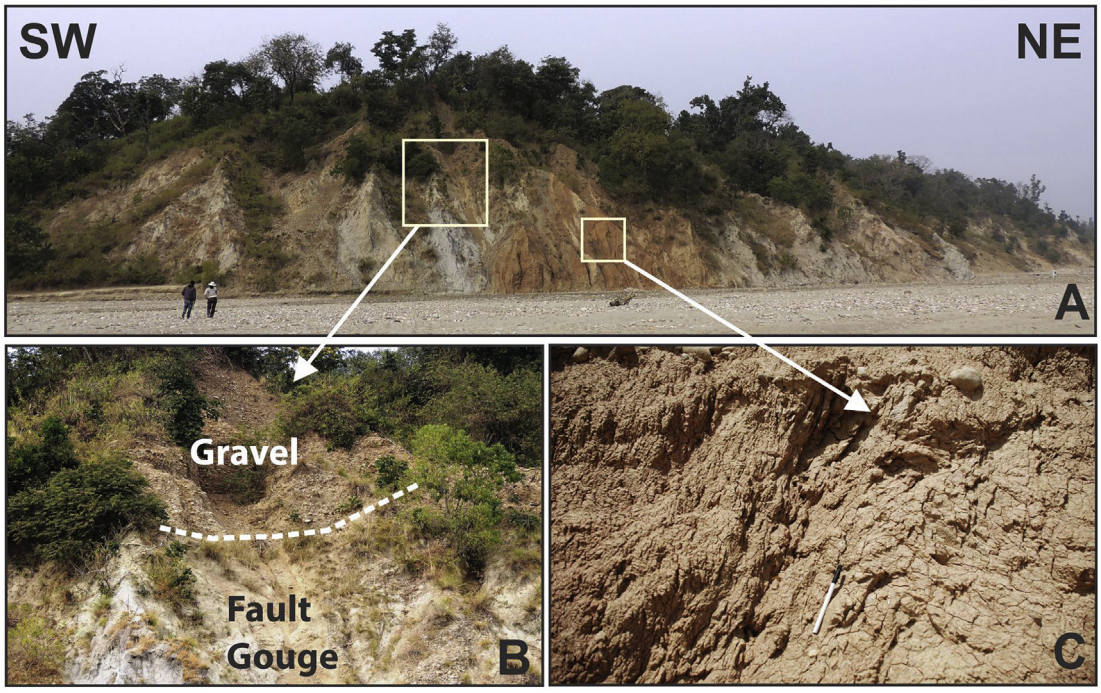

Fig. 7. Frontal topography and MFT fault core exposed along the Khajnawar Rao (3 in Fig. 3). (A) ~700-m-wide outcrop of the MFT fault core and damage zone. People (~1.5 m) in lower left for scale. (B) Quaternary gravel overlying the fault gouge in the fault core. (C) Close up of highly pulverized fault gouge in the core. Standard pen for scale.

are likely to be inherited in the clasts eroded from a deformed provenance such as the MCT sheet as they are not systematically distributed. Closer to the fault zone (b in Fig. 3), in addition to the features described above, we saw an increase in matrix percentage

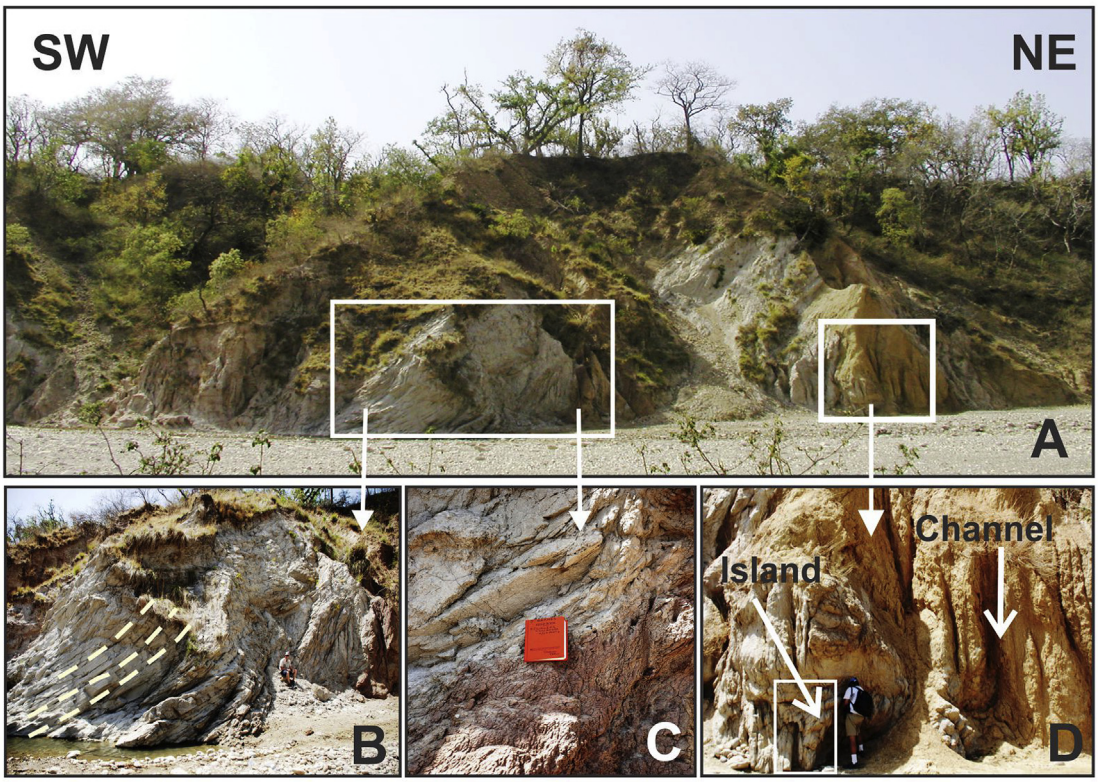

Fig. 8. MFT hanging wall damage zone exposed in the Khajnawar Rao. (A) Fault-gouge dominated fault damage zone containing meter-scale islands of fractured Middle Siwaliks rock. (B) Southwest-dipping relict bedding in a Middle Siwaliks island with a person for scale. (C) Fracturing and brecciation observed in islands in contact with red-colored, fine-grained gouge with a standard field note book for scale. (D) Islands of fractured rocks and channels of pulverized rock within the gouge-dominated fault zone with a person (~1.7 m) for scale. Notice the gully erosion of the pulverized channel material.

and the frequency of intracrystalline fractures (Fig. 11B). Matrix dominated the rock within the island in the fault damage zone (c in Fig. 3). We also observed a marked increase in the number of intracrystalline and transgranular fracturing (Fig. 11C) resulting in decrease of the framework grain sizes within the fault damage zone. The mean grain-size measured in sections oriented parallel to the regional NE-SW direction decreased from 47.97 in the protolith (Fig. 12A) through 24.57 in the fault related damage zone (Fig 12B) to 17.91 $\times$ 10^{-5} cm^2 in the islands in the fault zone (Fig. 12C), respectively. Fault zone petrography, deformation microstructures and grain-size analysis, together with field observations, provide constraints on the deformation mechanisms in the MFT fault zone and the appropriate rheology to model deformation and related topographic growth.

4.6. Mohand Range topography

Topographic profiles across the Mohand Range using SRTM C-Band 90 m resolution data reveal a ~4 km wide maximum relief (350–500 m) zone in the central Mohand Range (Barnes et al., 2011). Present-day ellipsoidal elevations along the central Mohand Range based on the RTKGNSS data, along the road section of Mohand Rao River are between ~400 and 750 m (datum WGS84). The highest elevation measured along the traverse near the drainage divide was 725 m with a maximum relief of ~325 m from the present-day drainage divide to base level (~400 m) at the southwestern mountain front. Base level at the northern flank of the mountain was ~600 m. This suggests there was a pre-existing foreland slope of ~0.64° from which the Mohand topography emerged based on RTKGNSS measurements in the Dun away from fans, in the river valley within the Mohand Range and south of the Mohand Range (Fig. 13). There has been no active sedimentation in the Dun Valley since 16 ka (Densmore et al., 2016) so the pre-existing slope would be stable after that. We estimated ~2.3 km^2 of topography above the southern ~400 m base level along the measured traverse in profile; 0.8 km^2 southwest of the divide and 1.5 km^2 northeast of it. Using a pre-existing foreland with 0.64° slope, we estimated an area of 1.1 km^2 above the base (Fig. 13); 0.5 km^2 southwest of the divide and 0.6 km^2 northeast of it. Interestingly, the MFT fault zone is exposed ~10 km southwest of the NW-SE-oriented drainage divide, in places even past the southwestern topographic front (Figs. 3 and 13). Thus, the exposed MFT fault zone is not directly associated with the major part of the present-day Mohand Range topography indicating that either the topography has receded away from the fault or the fault has propagated southwestward from the topography. This fact is an important geometrical constraint for kinematic models of fault-related topographic growth in the Mohand Range.

5. Discussion

5.1. MFT fault zone geometry and kinematics

Observations across 4 traverses along the southwestern front of the Mohand Range clearly indicate the MFT is emergent in the western portion of the range. However, only the hanging wall damage zone is exposed and the MFT fault core and damage zone exposure extend to a maximum strike-perpendicular length of ~700 m from the mountain front. The exposure length of the fault core varies from a maximum of ~250 m in the central range to

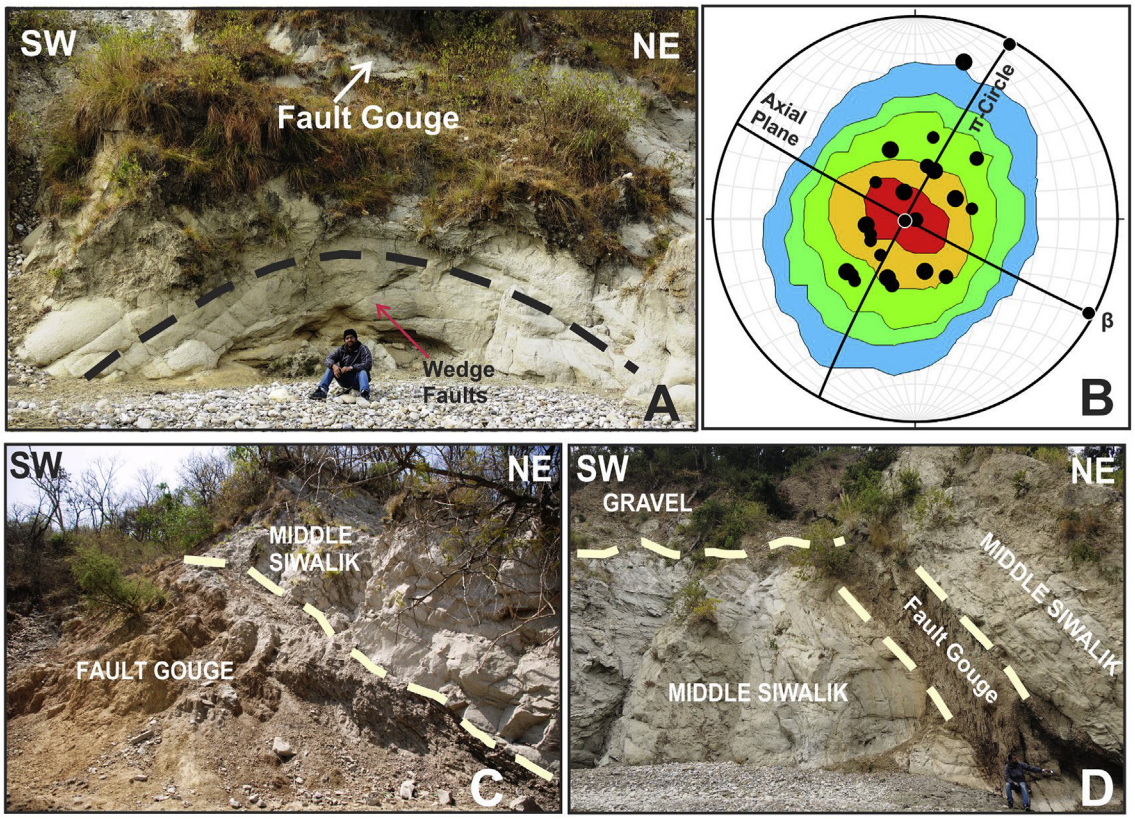

Fig. 9. Rock-dominated MFT fault damage zone in the Khajnawar Rao. (A) Intact, meter-scale fold preserved in Middle Siwaliks rock near transition from gouge-dominated to rock-dominated hanging wall fault damage zone with a person for scale. (B) Structural data (25 poles to bedding) in the frontal part indicating presence of upright, non-plunging folds with near vertical axial plane 298°/75° NE and fold axis (β) 0° → 118°. The π-circle is the great circle along which poles to bedding lie. (C) Consistently northeast-dipping beds in the MFT hanging-wall damage zone showing meter-scale gouge. (D) Thin (dm-scale) bands of fault gouge within fractured outcrops of Middle Siwaliks sandstones near the north-eastern edge of the fault zone with a person for scale.

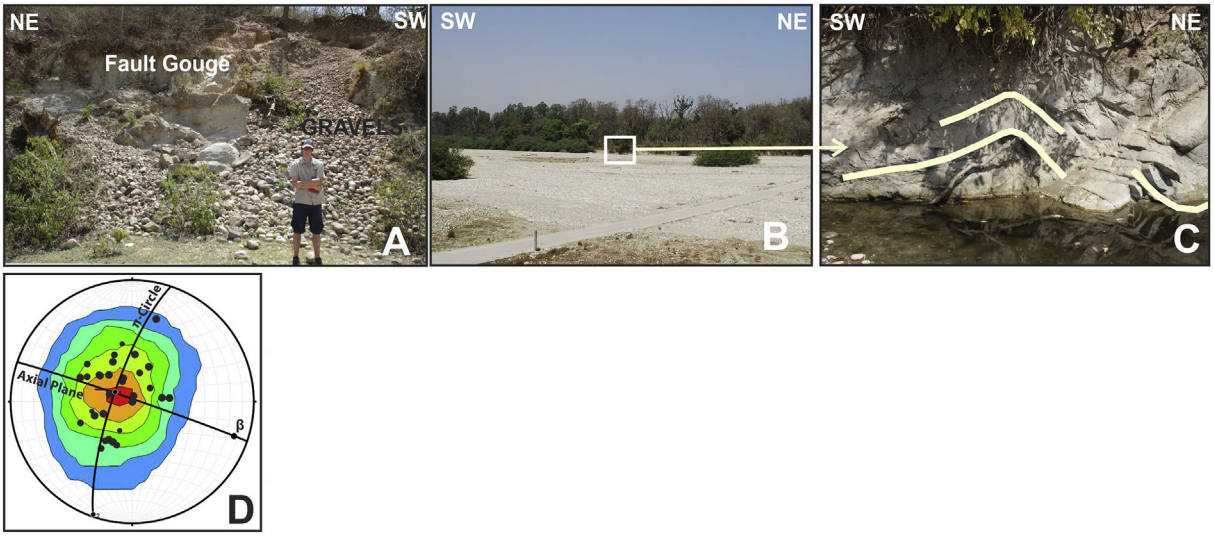

Fig. 10. The MFT fault zone and its proximal hanging wall in the Mohand Rao. (A) MFT-related, 15–20 m-wide fault gouge along the eastern channel bank near the mountain front. (B and C) Outcrop scale, upright non-plunging fold along the eastern bank with a standard geological hammer (~30 cm) for scale. The road in (B) is ~4 m wide. (D) Structural data (31 poles to bedding) from the proximal hanging wall indicating presence of upright, non-plunging folds with near vertical axial plane 288°/88°NE and fold axis (β) 13° → 118°. The π-circle is the great circle along which poles to bedding lie.

~15–20 cm in the northwestern region near the Yamuna River and to ~10–15 m to the southeast near Mohand (Fig. 3). This suggests a progressive thickening from northwest to southeast (from the Barkala to the central range), then subsequent thinning farther to the southeast in the Mohand Rao. Thickness increase in a fault zone shows a broad correlation with fault displacement, although

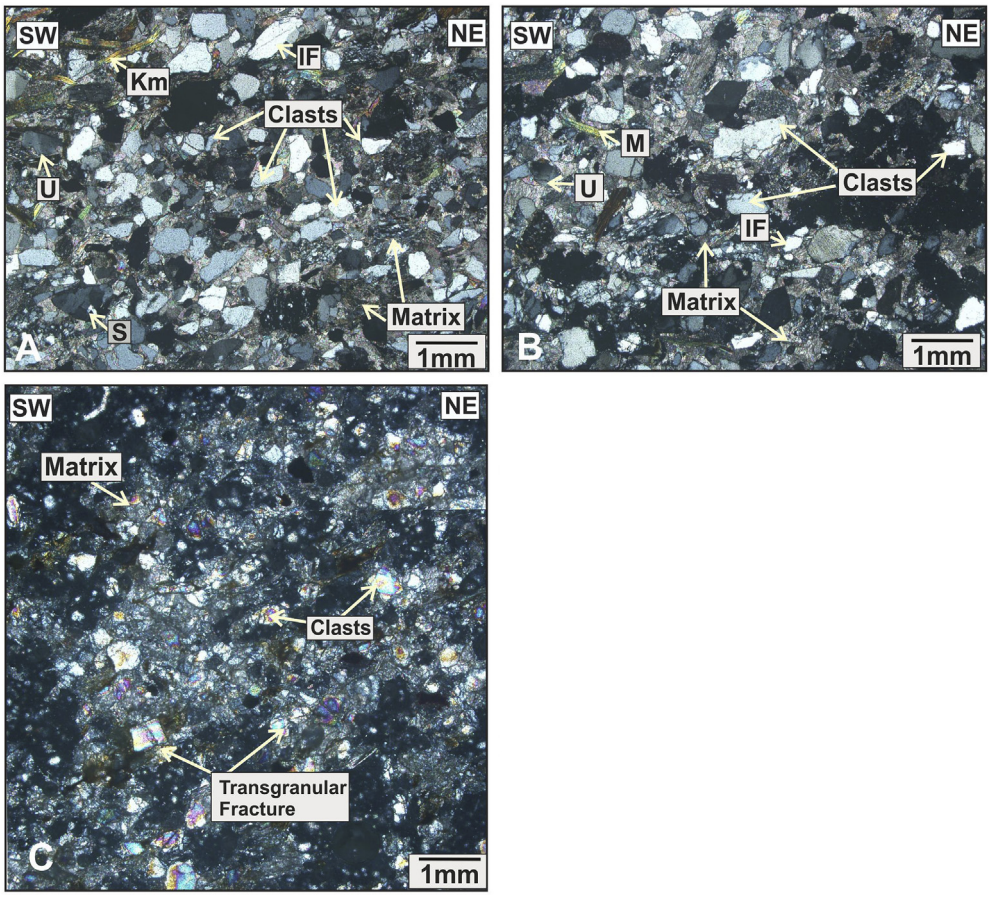

Fig. 11. Petrography and deformation microstructures in Middle Siwaliks sandstone adjacent to the MFT fault zone. (A) The sandstone outside the fault zone exhibits dominantly quasi-plastic microstructures that are likely inherited from its high grade provenance in the rocks of the MCT thrust sheet. (B) Sandstones closer to the fault zone show elastico-frictional microstructures and a marginal increase in matrix content and intragranular fracturing (IF) (C) Matrix dominates the rock in the islands of the MFT damage zone with a marked decrease in clast grain size. U = Undulose extinction, Km = Kink Mica, M = Mica, S = Subgrain. Sample locations shown as a-c in Fig. 3.

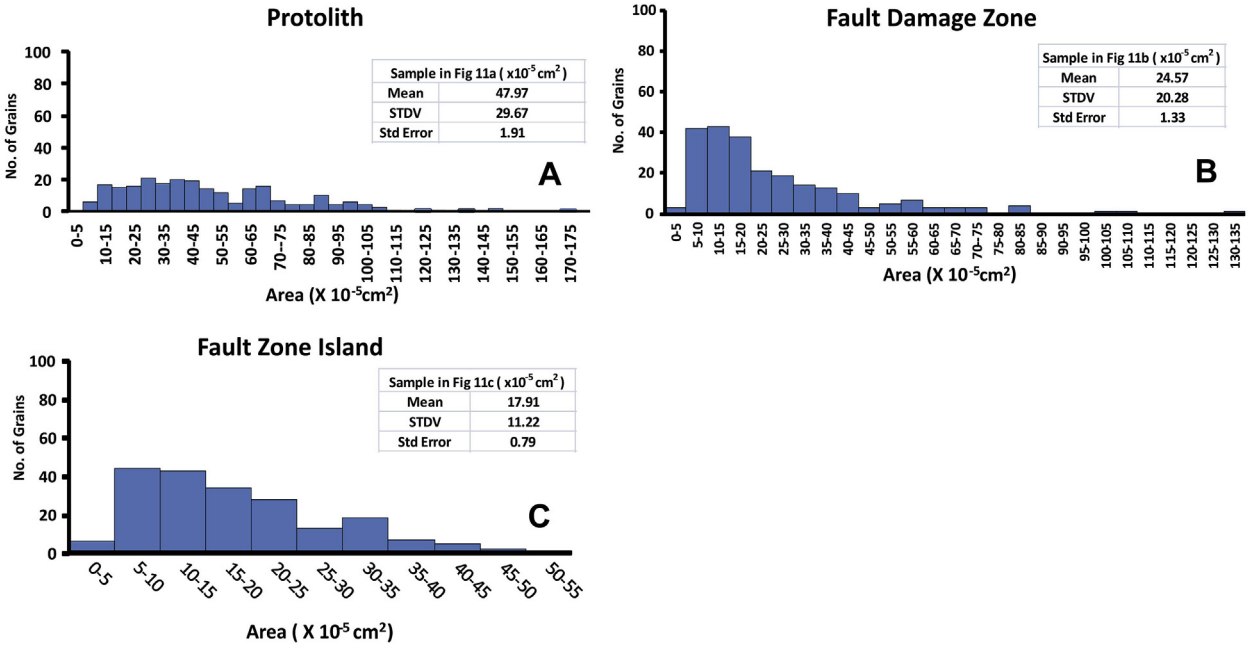

Fig. 12. Histograms showing grain size variations in samples from Mohand range corresponding to locations a, b, c in Figs. 3 and 11 A, B, and C.

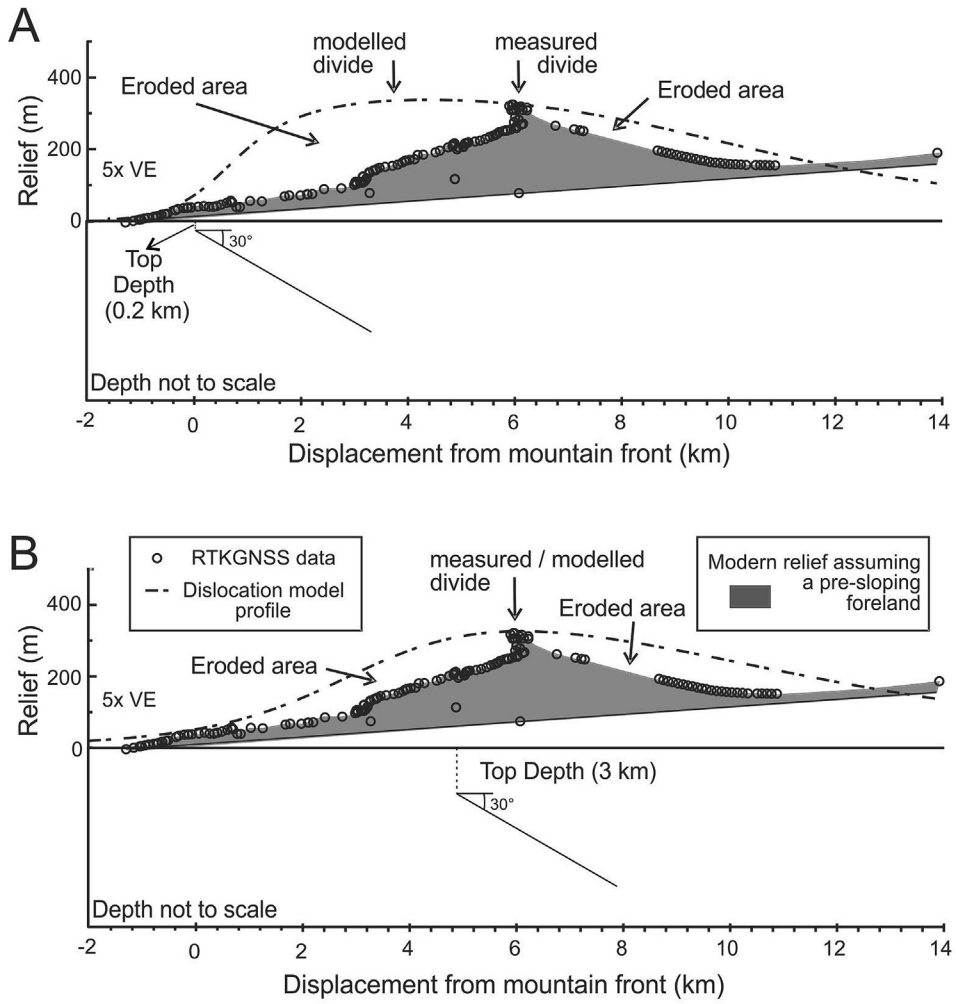

Fig. 13. Measured vs. modelled topographic profiles across the central Mohand Range (locations in Fig. 3). (A) Case 1: near-surface, frontal dislocation model and (B) Case 2: blind dislocation model. The projected surface trace of the dislocation is ~1 km southwest of the mountain front (x = 0) for Case 1 and near the front in Case 2. Note that the estimated eroded areas are asymmetric in A and symmetric in B relative to the measured data. The gray base line is an estimated pre-existing foreland slope of 0.64° (see explanation in text). Subsurface locations of faults are not to scale (after Myers et al., 2003; Watters et al., 2002, Watters, 2004).

increase in thickness may also be controlled by (i) fault zone and wall-rock rheologies (e.g. strain-hardening in phyllosilicate-rich rocks or porous sandstones or a simple variation in lithology within a fault zone (Aydin and Johnson, 1983; Faulkner et al., 2003)), and/or (ii) fault structure inherited from the geometry of the initial fault array and the way slip is heterogeneously accommodated in the fault zone leading to development of core/damage zone geometry (Caine et al., 1996; Rawling et al., 2001; Billi et al., 2003) or a fault zone strongly affected by the scale of initial fault segmentation and fault surface irregularity (Childs et al., 2009). In most cases, increase in displacement is accompanied by increase in fault thickness as the zone of deformation progressively widens through time. The MFT fault zone geometry suggests that it underwent maximum displacement in the central range near the Kaluwala and Khajnawar sections as fault zone thickness scales with displacement (Fig. 3) (e.g. Marrett and Allmendinger, 1990; Shipton and Cowie, 2003; Wibberley et al., 2008), although probably by progressive incorporation of fault rock by continuous migration of the wall rock/fault rock interface wall in the Middle Siwalik sandstones (Faulkner et al., 2003; Bonson et al., 2007) as evident from large islands of wall rock in the damage zone.

We observed uplifted, gravel strath terraces overlying the fault zone ~10–15 m above the present stream level near the mountain front. The gravels yielded a 0.0037 ± 0.00022 Ma charcoal-based radiocarbon date in an uplifted fluvial terrace (Wesnousky et al., 1999). The terraces overlay the fault gouge for the entire ~700 m length of the exposure from the mountain front (Wesnousky et al., 1999). Beyond the fault zone, the terraces abruptly disappeared and fractured, northeast-dipping Middle Siwaliks sandstones dominated the outcrops. These observations imply that emergent MFT fault zone deformation uplifted the gravel under near surface, elastico-frictional conditions with little overburden at ~1–5 km depth (Sibson, 1977). We use deformation microstructures to test this hypothesis further.

Deformation microstructures from Middle Siwaliks quartz grains outside the fault zone suggest that the overall deformation regime is quasi-plastic with stable fracturing (Blenkinsop, 2000; Passchier and Trouw, 2005). However, lithoclasts with mylonitic elongated quartz grains show that quasi-plastic deformation microstructures within the clasts or framework grains may be inherited from a highly deformed provenance such as the MCT fault zone and not from quasi-plastic deformation within the MFT sheet. Islands of less deformed rocks in the MFT damage zone, however, show an increase in matrix percentage and frequency of intracrystalline fractures that overprint the quasi-plastic features. The existence of elastico-frictional deformation features such as micro-

fracturing and pressure solution seams that we described above support the interpretation (Srivastava and John, 1999) that MFT deformation occurred under near surface, elastico-frictional conditions (Sibson, 1977).

We observed meter-scale, upright, non-plunging, symmetric, antiform-synforms instead of consistently southwest-dipping beds (Raiverman et al., 1994; Thakur, 1992; Wesnousky et al., 1999; Mukhopadhyay and Mishra, 2004) in the proximal MFT hanging wall. Because deformation in the MFT occurred at ~1–5 km depths, we interpret this folding to result from accommodation of shortening by cataclastic flow (Ismat and Mitra, 2005; Passchier and Trouw, 2005) under near-surface conditions near the MFT as evident from wedge faults seen in the hinge zone of these folds (Fig. 9A). Also, these folds are m-folds with a sub-horizontal enveloping surface because they are symmetric, non-plunging, and upright (Figs. 5, 6G, 9A and B, 10D). Taken together, these data show that in the western Mohand Range, there is no evidence for a southwest-dipping limb of the Mohand antiform. Thus, we recommend the Mohand Range no longer be referred to as an antiform or anticline as has been commonly reported for a long time (e.g. Karunakaran and Ranga Rao, 1979; Mishra and Mukhopadhyay, 2002). We, therefore, anticipate that the 1st-order structure exposed in the western Mohand Range is not an anticline and its detailed geometry and kinematics needs to be revisited primarily because a range-scale, southwesterly-dipping limb is absent.

We also observe that the meter-scale m-folds in the proximal MFT hanging wall have become disconnected in the MFT fault zone in the Khajnawar Rao (location 3 in Fig. 3) where the fault zone is widest. There are disconnected folds in the islands observed in the fault zone that are separated by fault gouge. In some islands, only one of the fold limbs is preserved (Fig. 8B). In others, either the antiform or the synform is preserved (Fig. 9A). We interpret these features to indicate that the folds formed first and were initially intact. The MFT then propagated through these folds and dismembered them. Relict parts of pre-existing structures are also preserved in the islands. Farther to the northeast, the folds are continuous but cross-cut by zones of fault gouge similar to transects east and west of Khajnawar Rao where the MFT fault zone is thinner. This also implies that the folds formed first, probably to accommodate shortening at the tip of the propagating MFT, and were subsequently cut by it (e.g. McNaught and Mitra, 1993). This is an important point because fold dismemberment at a propagating fault tip would not occur in a fault-bend fold. In the Barkala and Mohand Rao, the fault propagated in a manner such that the folds were preserved in the hanging wall and not dismembered, perhaps because the fault zone was thinner there. In summary, our new data collectively indicate that a fault-propagation fold structural model associated with an emergent MFT (e.g. Powers et al., 1998) better describes the MFT-uplifted Mohand Range compared to a fault-bend fold involving a blind MFT (e.g. Mishra and Mukhopadhyay, 2002).

5.2. MFT fault zone conceptual model in the Mohand Range

The most complete exposure of the MFT fault zone was observed in the Khajnawar Rao section and provides the foundation for a conceptual model of MFT fault zone deformation (Fig. 14). First, our observations indicate that MFT-related deformation in the emergent fault zone occurred in the elastico-frictional regime and the grain-size reduction mechanism was unstable fracturing. Second, in a quasi-plastic island-channel model of shear zones (Newman and Mitra, 1993), (a) islands are essentially thick, deformed areas within a fault zone that minimizes fluid infiltration into the surrounding rocks, and (b) channels are thin, deformed areas with high fluid infiltration into the surrounding rocks. We extend the island-channel analogy to elastico-frictional fault zones and envision islands as resistant, less deformed parts of the host rock (e.g. Fig. 8D) surrounded by fine-grained, highly deformed gouge in the channels through which fluids can flow preferentially (Fig. 7B and C, 8D). Using this island-channel analogy, we distinguish three distinct zones within the MFT fault and damage zone with increasing distance from the mountain front (e.g. Fig. 14):

1. **Fault Core**: A 15-cm to 250-m horizontal zone of fine-grained powdery gouge (Figs. 4B and 6A-D, 7, and 14), with centimeter-scale islands scattered throughout. These gouges in places, are colored red through oxidation by weathering processes (Figs. 6B and 7A, C). The core is exposed in the Barkala, Kaluwala and Khajnawar Rao sections and represents the zone of maximum grain-size reduction throughout the MFT fault zone (Figs. 4B and 6A-D, 7).
2. **Gouge-Dominated hanging-wall fault damage zone**: An ~300 m horizontal zone dominated by channels of fine-grained gouge that surround meter-scale islands of less-deformed, fractured, and matrix-dominated (Fig. 11C) sandstones with relict bedding (Fig. 8B) and folds within them. The fact that gouge channels surround the islands (Fig. 8D), shows that the overall fabric of the rock is gouge dominated (Fig. 14). This zone is partially preserved in the Kaluwala section (e.g. Figs. 1A and 6E, F).
3. **Rock-Dominated hanging wall fault damage zone**: An ~150 m horizontal zone characterized by northeast-dipping, fractured Middle Siwaliks sandstones with minor zones of fault gouge intermixed (Fig. 9). This zone is devoid of island-channel geometries and is only exposed in the Khajnawar Rao section. Beyond this zone, fractured, northeast-dipping Middle Siwaliks sandstones dominate (Fig. 11B).

The kinematic relationship between the fault zone folds and faulting provides field-based limits on MFT-related topographic growth. In the fault core, extreme grain-size reduction results in the formation of powdered fault gouge that obliterates pre-existing structures. In the gouge-dominated damage zone, there are dismembered folds only in the islands separated by the gouge in the channels. Relict parts of pre-existing structures are preserved in the islands. In the rock-dominated damage zone, folds are continuous, but cross cut by zones of fault gouge similar to transects east and west of Khajnawar Rao where the MFT fault zone is thinner. Dismembering and cross-cutting of meter-scale folds by MFT-related gouge is a clear indication of fault-propagation folding where slip accommodation at the propagating fault tip results in folds being cross cut by the subsequent propagation of the fault through them (e.g. McNaught and Mitra, 1993; Wallace and Homza, 2004; Tavani and Storti, 2011; Brandes and Tanner, 2014). In the following section, we invoke a fault-propagation fold model to simulate MFT-related topographic growth across the Mohand Range.

5.3. MFT-related Mohand Range topographic growth

Previously, the Mohand Range topography was postulated to have developed by MFT-generated uplift within ~5 km of the fault tip by fault-bend folding (Mishra and Mukhopadhyay, 2002; Mukhopadhyay and Mishra, 2004). This model also necessitates significant total rock erosion (~13 km^2) since faulting began because only ~15% of that total (~1.7 km^2) was represented in the existing relief profile (Fig. 2D; Barnes et al., 2011). However, our new observations support fault-propagation folding with the following characteristics; (a) the fault zone is exposed ~10 km

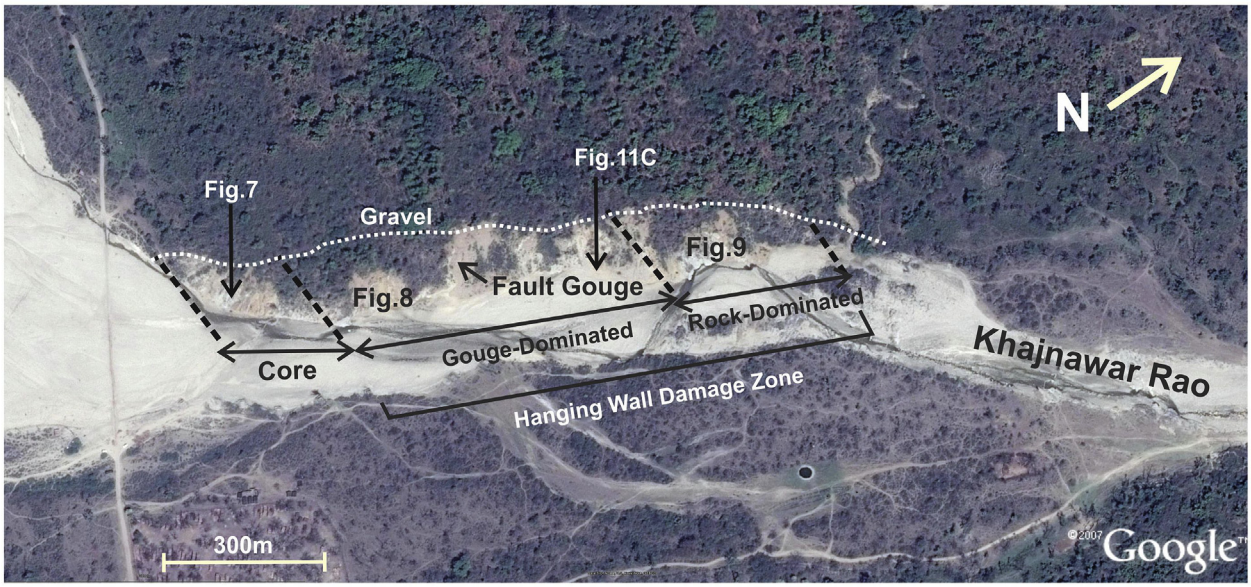

Fig. 14. Conceptual model for the MFT fault zone in the Mohand Range as best exemplified in the Khajnawar Rao (location 3 in Fig. 3). The fault core and hanging wall damage zone regions are exposed and the footwall damage zone remains buried. The fault core is characterized by powdered, unconsolidated fault gouge and the hanging wall damage zone by a (1) frontal gouge-dominated zone where meter-scale islands of less deformed rocks are scattered within it and then (2) a rock-dominated zone with fault gouge bands between largely intact, but fractured Middle Siwaliks rocks.

southwest of the present-day divide in the Mohand Range (Fig. 3), (b) meter-scale folds in the proximal MFT hanging wall have been crosscut by the MFT (Fig. 8), and (c) lack of field evidence for a prominent southwest-dipping limb associated with a first-order fold in the western Mohand Range. In general, a fault-propagation fold involves excess slip accommodation at the propagating fault tip because the propagation velocity is less than the slip along the fault itself (McNaught and Mitra, 1993; Brandes and Tanner, 2014). For thrust faults, this excess slip can break the surface and generate topography (e.g. Ellis and Densmore, 2006; Seong et al., 2011).

The Mohand Range could have evolved in two possible ways during fault-propagation folding. First, it could have been generated near the present-day location of the emergent MFT. This scenario implies that the present-day fault-related frontal scarp was formed to the southwest of its current location and erosion removed material immediately adjacent to the surface outcrop of the fault, causing the drainage divide to retreat to its present position (e.g. Gupta and Ellis, 2004) 10 km north of the present rangefront (Fig. 13A). Alternatively, the topography was generated close to where it is today north of the surface expression of the fault. If the present-day topography mirrors the location of the topographic growth, this implies that the MFT has moved through time and propagated to the southwest, and ahead of, the main topographic front. This scenario could also result if off-fault deformation (e.g. flexural-slip/buckling) plays a large role in generating the topography in the Mohand Range. To distinguish between these various options requires more information about the amount of erosion and off-fault deformation. However, we use numerical modelling to obtain insight into more focused questions and the data that would enable us to determine which one of the various scenarios is most likely. Off-fault deformation by accommodation of shortening only by folding and cleavage formation in the MFT sheet is unlikely as the topography has only been generated in the Mohand Range and strata remains flat north of it in the Dehra Dun for ~12 km. Off-fault folding should fold the entire hanging wall of the MFT. Moreover, we did not see evidence of significant bedding plane slip or buckling (Huang and Johnson, 2016) in the field or reported in the literature that could explain the large scale topography of the Mohand Range. However, we acknowledge that the slip along the MFT could be accommodated by flexural-slip folding within the Mohand Range and the second-order folding of Middle Siwalik rocks in the MFT fault zone is most likely off-fault. However, these folds are only seen near the MFT exposures ~2 km south of the Mohand Range topography and have a horizontal enveloping surface capped by Quaternary gravels that suggests that they could not have contributed significantly to the topography of the Mohand Range. So unless new data points to significant contribution of off-fault folding topography in the Mohand Range, we focus our attention to fault propagation folding scenarios only.

The questions we explore through the modelling relate to coupling between the MFT and the range topography. Is the Mohand Range topography coupled with slip and propagation of the MFT or not? How much of it has been eroded subsequent to its formation necessitating drainage-divide retreat? We address these questions with a dislocation model to evaluate between two end-member scenarios (MFT as near surface and blind) involving fault-related folding, and compare the results against existing tectonomorphic observations of Mohand Range topography, faulting, and geologic structures (detailed below in the discussion) wherein slip along a causative dislocation (fault proxy) generates a surface-displacement field ahead of the propagating fault tip. Furthermore, the vertical component of this displacement field is the topography that can be considered as the fault-generated landscape. Finally, we compared this landscape simulation with RTKGNSS profile data to evaluate the relationship between the MFT-generated topography and the present-day morphology and erosion across the Mohand Range.

We modelled the scenarios in two separate cases as follows (Figs. 3 and 13). In Case 1, we assumed the entire topography was developed by slip along a dislocation located near the present-day MFT location. In Case 2, we examine the possibility that the topography and tectonics are decoupled. In other words, the

topography could have developed when the MFT was located north of its present day position near the modern drainage divide, then subsequently propagated to its present position with minimal slip contribution to the main topography. In both cases, we then compared measured and modelled topographic profiles to better discern the kinematics, geometry, and evolution of the MFT and Mohand Range topography.

5.4. Simulated vs. measured topographic growth

In Case 1, we used a near-surface, frontal dislocation model to generate slip along a dislocation trending 140-320° with a moderate 30°NE dip to simulate a topographic profile, unmodified by erosion, across the Mohand Range (Table 1; Fig. 13A). Results show generation of a maximum relief of 337 m and a minimum total topographic area of 3.4 km^2 above the 400 m base level at the southwestern mountain front. This area was ~0.5 km^2 southwest of the modelled divide and ~2.9 km^2 northeast of it. When we consider a pre-existing foreland slope of 0.64°, the total modelled area above it was 2.3 km^2, of which ~0.5 km^2 was southwest of the modelled divide and ~1.8 km^2 northeast of it. We compared the relief estimates to quantify the effect of erosion and found that the maximum relief was reduced from 337 to 324 m. The flat-base model necessitates significant erosion along the present-day southwestern slope (eroded area = 0.9 km^2) of the Mohand Range and escarpment retreat by ~3–5 km as compared to the northeastern slope (eroded area = 0.3 km^2) (Fig. 13A). This implies a minimum, total erosion of ~1.2 km^2 in the central Mohand Range. Furthermore, the highest elevation has retreated by ~4 km to the northeast. About 2.2 km^2 of the initial 3.4 km^2 of topographic area (~65% of the total) remained preserved above the 400 m base level. In the foreland slope model, 1.1 km^2 of the 2.3 km^2 of topographic area (~48% of the total) was preserved. These erosion values were substantially lower than current estimates (1.2 vs. 13 km^2 eroded; 57% vs. 15% topography preserved) based on a fault-bend fold model (Fig. 2D; Barnes et al., 2011). In our case, the modelled topography was asymmetric with the southwest-facing slope shorter and steeper (7.8° slope) than the northeastern slope (2° slope) (Fig. 13A). Erosional retreat and degradation of the southwestern topographic front reduces the gradient from 7.8 to 2.2° (compare profiles in Fig. 13A). In contrast, the northeastern slope gradient is hardly modified by erosion, changing from 1.8° to 2°.

In Case 2, we used a blind, near-drainage-divide dislocation model to generate slip along a dislocation with the same orientation as Case 1 to simulate another topographic profile (Table 1; Fig. 13B). Results show a maximum relief that is ~326 m with little change in altitude (~324 m) or location due to erosion. The simulated topography was symmetric and generated ~3.1 km^2 of topographic area in profile with ~2.1 km^2 of it northeast of the divide and 1.0 km^2 southwest of it above the 400 m base level at the mountain front (Fig. 13B). In the foreland slope model, the total simulated topography above the base was 2 km^2 and it was equally distributed on either side of the modelled divide. Northeastern and southwestern slopes of the modelled topography had slopes of 1.6° and 3.7°, respectively. This result required a minimum erosion of ~0.4 km^2 along both slopes of the Mohand Range and a topographic front retreat by ~1–2 km. Interestingly, the drainage divide remained unchanged in its position and ~75% of the initial topography remained preserved. Retreat and degradation of the southwestern topographic front resulted in the reduction of the gradient from 3.7° to 2.2° (Fig. 13B). In contrast, the gradient of the northern slope was not appreciably modified and only changed from 1.6° to 1.8° after erosion.

Dislocation modelling of MFT-related topographic growth for the Mohand Range using two possible fault-propagation folding scenarios provided insightful distinctions. The first scenario (Case 1) generated asymmetric topography with a 4xs steeper slope facing the southwest (Fig. 13A). In contrast, Case 2 generated symmetric topography that resembled the measured present-day topographic profile more closely with the southwest-facing slope only 2xs as steep. Compared to the modern geomorphology, the topography generated in Case 1 was far more dynamic than in Case 2 because (a) the drainage divide and southwest-facing escarpment had migrated northeastward through time, and (b) almost 3xs as much erosion was required on the frontal flank of the range (Fig. 13A). There was also a higher coupling between the topography and tectonics in Case 1 because the bulk topographic growth occurs near the present, emergent position of the MFT. Case 2 suggested a static divide and substantial topographic preservation that is at odds with existing studies (e.g. Gupta and Ellis, 2004; Barnes et al., 2011), thus Case 1 might appear more likely than Case 2. However, field evidence (Figs. 4, 7B and 10A) clearly indicated that the entire emergent MFT fault zone was capped by uplifted Quaternary gravels that created a strath surface. This implied that the fault zone was intact and not eroded. The gravels also helped rule out the presence of overlying beds in the MFT fault zone. Presence of powdery, unconsolidated fault gouge in the fault zone (Figs. 6, 7, 8, 10A) also suggested a lack of substantial overburden over the emergent fault zone. The evidence, thus, suggests that the emergent MFT propagated southwest and ahead of the present-day Mohand topography without much overburden over it. The reality may be a combination of the two end-member scenarios and independent datasets, especially erosion rates from both flanks of the Mohand Range, are needed to further constrain this aspect of the evolution of the MFT related deformation and topographic growth of the Mohand Range.

6. Summary and conclusions

Our study exploits newly discovered exposures of the Main Frontal thrust (MFT) fault zone to develop improved insights into the geometry, kinematics, evolution, and associated topographic growth of the Mohand Range in northwest India. We summarize our main results as follows: (1) The MFT is exposed along 4 traverses across the southwestern topographic front of the Mohand Range. This establishes that the MFT is an emergent fault. Here, the MFT daylights ~10 km south of the present-day range divide and is capped by Quaternary gravels that have been uplifted above the present-day streambed by ~10–15 m. (2) The width of the MFT fault zone exposure is variable in space. The core varies from northwest to southeast across the study area as follows: ~15–20 cm to ~150–250 m, then to ~10–15 m. This suggests maximum deformation and displacement occurred near the center consistent with fault length-displacement scaling laws between the central and the northwestern Mohand Range. (3) The fault zone has several components consistent with modern fault zone framework. It exhibits a well-defined fault core that transitions into a hanging wall fault related damage zone. The fault core and frontal part of the hanging wall damage zone are dominated by fault gouge and exhibit island-channel geometries. The footwall damage zone is not exposed. (4) Incohesive fault gouge, breccia, and fracturing along with deformation microstructures, such as transgranular microfracturing and an increase in matrix percentage, indicate the fault zone has experienced near-surface (~1–5 km depth), elastico-frictional deformation. (5) Outcrop scale, non-plunging, upright with near vertical axial plane antiforms and synforms exist in the proximal hanging wall. Some folds are dismembered in the fault zone indicating that they developed before the fault propagated through them, thus fault-propagation folding was the likely mechanism for topographic growth in the Mohand Range. (6) High-resolution,

real-time, satellite–based topographic measurements across the central Mohand Range quantify a maximum relief of ~324 m near the present-day drainage divide that currently preserves ~1.1–2.3 km^2 of topographic area in profile. (7) Dislocation model results help confirm that MFT-related topography across the Mohand Range was most probably developed by fault-propagation folding. The topography grew either by fault propagation folding on an emergent MFT near its present location or a blind MFT near the present-day divide or some combination of these two scenarios. (8) Comparison of modelled and measured topography provides us with two possible end-member scenarios that can be further tested with more data. Either the MFT-related topography dynamically evolved by differential erosion along its two slopes with northeastward migration of the southwestern escarpment and divide or it was static and subjected to symmetric and minimal erosion.

In summary, our study is the first detailed record and analysis of MFT fault zone deformation that integrates geological field data, fault zone theory, deformation microstructures, digital topographic measurements, and dislocation-based numerical modelling to constrain deformation and coupled topographic growth at the Himalayan front. Our approach improves understanding of MFT deformation and topographic growth across the entire Himalayan front with implications for active, collisional wedge development, and associated seismotectonic hazards globally.

Acknowledgments

We thank Jack Pickering, Vimal Singh, Vikrant Jain, and Rahul Kaushal for their assistance in the field. VS acknowledges funding from Indian Institute of Technology Bombay through a Teaching Assistantship at the Department of Earth Sciences. This work was also supported by grants NSF EAR 0814723 to JB and DST SR/S4/ES-415/2009 to MM. Excellent critical reviews by two anonymous reviewers and Editor Ian Alsop helped greatly improve the quality of the manuscript. We also benefitted from discussions with Prof. S. K. Tandon.

Supplementary data

Supplementary data related to this article can be found as Appendix A and Appendix B at http://dx.doi.org/10.1016/j.jsg.2016.10.009.

References

Aki, K., 1989. Geometric Features of a Fault Zone Related to the Nucleation and Termination of an Earthquake Rupture. United States Geological Survey Open-File Report 89-315, pp. 1–9.
Allen, G.H., Barnes, J.B., Pavelsky, T.M., Kirby, E., 2013. Lithologic and tectonic controls on bedrock channel form at the northwest Himalayan front. J. Geophys. Res. Earth Surf. 118, 1–20. http://dx.doi.org/10.1002/jgrf.20113.
Avouac, J.P., 2003. Mountain building, erosion, and the seismic cycle in the Nepal Himalaya. Adv. Geophys. 46 http://dx.doi.org/10.1016/S0065-2687(03)46001-9.
Aydin, A., 1978. Small faults formed as deformation bands in sandstone. Pure Appl. Geophys. 116 (4–5), 913–930.
Aydin, A., 1988. Discontinuities along thrust faults and the cleavage duplexes. Geol. Soc. Am. Special Publ. 222, 223–232.
Aydin, A., Johnson, A.M., 1983. Analysis of faulting in porous sandstones. J. Struct. Geol. 5, 19–31.
Bangen, S.G., Wheaton, J.M., Bouwes, N., Bouwes, B., Jordan, C., 2014. A methodological intercomparison of topographic survey techniques for characterizing wadeable streams and rivers. Geomorphology 206, 343–361.
Barnes, J.B., Densmore, A.L., Mukul, M., Sinha, R., Jain, V., Tandon, S.K., 2011. Interplay between faulting and base level in the development of Himalayan frontal fold topography. J. Geophys. Res. 116, 1–19. http://dx.doi.org/10.1029/2010JF001841. F03012.
Bendick, R., Bilham, R., 2001. How perfect is the Himalayan arc? Geology 29 (9), 791–794.
Bernhard, H.W., Herbert, L., Elmar, W., 2008. GNSS – Global Navigation Satellite Systems. Springer-Verlag Wien.
Bilham, R., Gaur, V.K., Molnar, P., 2001. Himalayan seismic hazard. Science 293.
Bilham, R., Blume, F., Bendick, R., Gaur, V.K., 1998. Geodetic constraints on the translation and deformation of India: implications for future great Himalayan earthquakes. Curr. Sci. 74, 213–229.
Billi, A., Salvini, F., Storti, F., 2003. The damage zone-fault core transition in carbonate rocks: implications for fault growth, structure and permeability. J. Struct. Geol. 25, 1779–1794.
Blenkinsop, T.G., 2000. Deformation Microstructures and Mechanisms in Minerals and Rock. Springer.
Bonson, C.G., Childs, C., Walsh, J.J., Schöpfer, M.P.J., Carboni, V., 2007. Geometric and kinematic controls on the internal structure of a large normal fault in massive limestones: the Maghlaq Fault, Malta. J. Struct. Geol. 29, 336–354.
Brandes, C., Tanner, D.C., 2014. Fault-related folding: a review of kinematics models and their application. Earth Sci. Rev. 138, 352–370.
Burgess, W.P., Yin, A., Dubey, C.S., Shen, Z.K., Kelty, T.K., 2012. Holocene shortening across the Main Frontal Thrust zone in the eastern Himalaya. Earth Planet. Sci. Lett. 357–358, 152–167.
Caine, J.S., Evans, J.P., Forster, C.B., 1996. Fault zone architecture and permeability structure. Geology 24, 1125–1128.
Cartwright, J.A., Trudgill, B.D., Mansfield, C.S., 1995. Fault growth by segment linkage: an explanation for scatter in maximum displacement and trace length data from the Canyonlands Grabens of SE Utah. J. Struct. Geol. 17 (9), 1319–1326.
Chester, F.M., Evans, J.P., Biegel, R.L., 1993. Internal structure and weakening mechanisms of the San Andreas Fault. J. Geophys. Res. 98, 771–786.
Childs, C., Manzocchi, T., Walsh, J.J., Bonson, C.G., Nicol, A., Schöpfer, M.P.J., 2009. A geometric model of fault zone and fault rock thickness variations. J. Struct. Geol. 31, 117–127. http://dx.doi.org/10.1016/j.jsg.2008.08.009.
Cladouhos, T.T., Marrett, R., 1996. Are fault growth and linkage models consistent with power law distributions of fault length? J. Struct. Geol. 18 (2/3), 281–293.
Cowie, P.A., Scholz, C.H., 1992. Physical explanation for the displacement–length relationship of faults, using a post-yield fracture mechanics model. J. Struct. Geol. 14, 1133–1148.
Cowie, P.A., Shipton, Z.K., 1998. Fault tip displacement gradients and process zone dimensions. J. Struct. Geol. 20 (8), 983–997. http://dx.doi.org/10.1016/S0191-8141(98)00029-7.
Crouch, S.L., Starfield, A.M., 1983. Boundary Element Method in Solid Mechanics. George Allen & Unwin, London.
Dawers, N.H., Anders, M.H., 1995. Displacement-length scaling and fault linkage. J. Struct. Geol. 17 (5), 607–614. http://dx.doi.org/10.1016/0191 -8141(94)00091-D.
DeCelles, P.G., Mitra, G., 1995. History of the Sevier orogenic wedge in terms of critical taper models, northeast Utah and southwest Wyoming. Geol. Soc. Am. Bull. 107, 454–462.
DeCelles, P.G., Gehrels, G.E., Quade, J., Kapp, P.A., Ojha, T.P., Upreti, B.N., 1998. Neogene foreland basin deposits, erosional unroofing, and the kinematic history of the Himalayan fold thrust belt, Western Nepal. Geol. Soc. Am. Bull. 110, 2–21, 0.1130/00167606(1998)110<0002:NFBDEU>2.3C); 2.
Delcaillau, B., Carozza, J.M., Laville, E., 2006. Recent fold growth and drainage development: the Janauri and Chandigarh anticlines in the Siwalik foothills, northwest India. Geomorphology 76, 241–256.
Densmore, A.L., Gupta, S., Allen, P.A., Dawers, N.H., 2007. Transient landscapes at fault tips. J. Geophys. Res. 112, 1–16. http://dx.doi.org/10.1029/2006JF000560.
Elliott, D., 1983. The construction of balanced cross-sections. J. Struct. Geol. 5, 101–115.
Ellis, M.A., Barnes, J.B., 2015. A global perspective on the topographic response to fault growth. Geosphere 11 (4), 1–16. http://dx.doi.org/10.1130/GES01156.1.
Ellis, M.A., Densmore, A.L., 2006. First-order topography over blind thrusts. In: Willett, S., Hovius, N., Fisher, D., Brandon, M. (Eds.), Climate and Landscape Evolution, Tectonics. Geological Society of America, vol. 398, pp. 251–266.
Evans, J.P., 1990. Thickness displacement relationships for fault zones. J. Struct. Geol. 12 (8), 1061–1065.
Faulkner, D.R., Lewis, A.C., Rutter, E.H., 2003. On the internal structure and mechanics of large strike-slip fault zones: field observations of the Carboneras fault in southeastern Spain. Tectonophysics 367, 235–251. http://dx.doi.org/10.1016/S0040-1951(03)00134-3.
Flinn, D., 1977. Transcurrent fault and associated cataclasis in Shetland. J. Geol. Soc. Lond. 133, 231–248.
Fossen, H., 2010. Structural Geology. Cambridge University Press, Cambridge.
Gansser, A., 1964. The Geology of the Himalayas. Wiley Interscience, New York.
Gansser, A., 1981. The geodynamic history of the Himalaya. In: Gupta, H.K., Delany, F.M. (Eds.), Zagros, Hindu Kush, Himalaya Geodynamic Evolution, vol. 3. American Geophysical Union, pp. 111–121.
Gleason, S., Gebre-Egziabher, D., 2009. GNSS Applications and Methods. Artech House.
Gudmundsson, A., 1992. Formation and growth of normal faults at the divergent plate boundary in Iceland. Terra Nova 4, 464–471.
Gudmundsson, A., 2011. Rock Fractures in Geological Processes. Cambridge University Press.
Gudmundsson, A., Simmenes, T.H., Larsen, B., Philip, S.L., 2010. Effects of internal structure and local stresses on fracture propagation, deflection, and arrest in fault zones. J. Struct. Geol. 32, 1643–1655. http://dx.doi.org/10.1016/j.jsg.2009.08.013.
Gupta, S., Ellis, M.A., 2004. Does the topography of actively growing folds mimic fold structure? The case of the Mohand anticline, frontal Himalaya. Geophys. Res. Abstr. 6, 06593.
Hodges, K.V., 2000. Tectonics of the Himalaya and southern Tibet from two

perspectives. Geol. Soc. Am. Bull. 112, 324–350.
Huang, W.J., Johnson, K.M., 2016. A Fault-cored anticline boundary element model incorporating the combined fault slip and buckling mechanisms. Terr. Atmos. Ocean. Sci. 2718, 73–85. http://dx.doi.org/10.3319/TAO.2015.06.18.01(TT).
Ismat, Z., Mitra, G., 2005. Folding by cataclastic flow: evolution of controlling factors during deformation. J. Struct. Geol. 27 (12), 2181–2203.
Jade, S., Mukul, M., Gaur, V.K., Kumar, K., Shrungeshwar, T.S., Satyal, G.S., Dumka, G.S., Jagannathan, S., Ananada, M.B., Kumar, P.D., Banerjee, S., 2014. Contemporary deformation in the Kashmir-Himachal, Garhwal and Kumaon Himalaya: significant insights from 1995-2008 GPS time series. J. Geodesy 88, 539–557.
Karunakaran, C., Ranga Rao, A., 1976. Status of Exploration for Hydrocarbons in the Himalayan Region—Con- Tributions to Stratigraphy and Structure. New Delhi, Him- alayan Geology Seminar, pp. 1–72.
Karunakaran, C., Ranga Rao, A.R., 1979. Status of exploration for hydrocarbon in the Himalayan region - contributions to stratigraphy and structure. Misc. Publ. Geol. Surv. India 41, 1–66.
Kim, Y.S., Sanderson, D.J., 2005. The relationship between displacement and length of faults. Earth Sci. Rev. 68, 317–334.
Kim, Y.S., Andrews, J.R., Sanderson, D.J., 2001a. Reactivated strike-slip faults: examples from north Cornwall, UK. Tectonophysics 340, 173–194.
Kim, Y.S., Andrews, J.R., Sanderson, D.J., 2001b. Secondary faults and segment linkage in strike-slip fault systems at Rame Head, southern Cornwall. Geosci. South West Engl. 10, 123–133.
Kim, Y.S., Peacock, D.C.P., Sanderson, D.J., 2004. Fault damage zones. J. Struct. Geol. 26, 503–517.
King, G.C.P., 1986. Speculations on the geometry of the initiation and termination processes of earthquake rupture and its relation to morphology and geological structure. Pure Appl. Geophys. 124, 567–585.
Kirby, E., Whipple, K.X., 2012. Expression of active tectonics in erosional landscapes. J. Struct. Geol. 44, 54–75. http://dx.doi.org/10.1016/j.jsg.2012.07.009.
Kumar, R., Ghosh, S.K., Sangode, S.J., 2003a. Mio-Pliocene sedimentation history in the northwestern part of the Himalayan Foreland Basin, India. Curr. Sci. 84 (8), 1006–1013.
Kumar, R., Ghosh, S.K., Mazari, R.K., Sangode, S.J., 2003b. Tectonic impact on the fluvial deposits of Plio-Pleistocene Himalayan foreland basin, India. Sediment. Geol. 158 (3–4), 209–234.
Kumar, S., Wesnousky, S.G., Rockwell, T.K., Ragona, D., Thakur, V.C., Seitz, G.G., 2001. Earthquake recurrence and rupture dynamics of Himalayan frontal thrust, India. Science 294, 2328–2331.
Kumar, S., Wesnousky, S.G., Rockwell, T.K., Briggs, R.W., Thakur, V.C., Jayangondaperumal, R., 2006. Paleoseismic evidence of great surface rupture earthquakes along the Indian Himalayas. J. Geophys. Res. 111 (B03304) http://dx.doi.org/10.1029/2004JB003309.
Kumar, S., Wesnousky, S.G., Jayangondaperumal, R., Nakata, T., Kumahara, Y., Singh, V., 2010. Paleoseismological evidence of surface faulting along the northeastern Himalayan front, India: timing, size, and spatial extent of great earthquakes. J. Geophys. Res. 115 (B12422), 1–20. http://dx.doi.org/10.1029/2009JB006789.
Lave, J., Avouac, J.P., 2000. Fluvial incision and tectonic uplift across the Himalayas of central Nepal. J. Geophys. Res. 106 (B11), 26561–26591.
Lave, J., Yule, D., Sapkota, S., Basant, K., Madden, C., Attal, M., Pandey, M.R., 2005. Evidence of a great Medieval earthquake (*1100 AD) in the Central Nepal. Science 307, 1302–1305.
Le Fort, P., 1975. Himalayas collided range-present knowledge of continental arc. Am. J. Sci. A275, 1–44.
Macedo, J., Marshak, S., 1999. The geometry of fold-thrust belt salients. Geol. Soc. Am. Bull. 111, 1808–1822.
Malik, J.N., Nakata, T., 2003. Active faults and related Late Quaternary deformation along the northwestern Himalayan Frontal zone, India. Ann. Geophys. 46 (5), 917–936.
Malik, J.N., Shah, A.A., Sahoo, A.K., Puhan, B., Banerjee, C., Shinde, D.P., Juyal, N., Singhvi, A.K., Rath, S., 2010. Active fault, fault growth and segment linkage along the Janauri anticline (fontal foreland fold), NW Himalaya, India. Tectonophysics 483, 327–343.
Marrett, R., Allmendinger, R.W., 1990. Kinematic analysis of fault-slip data. J. Struct. Geol. 12, 973–986.
Marshak, S., Mitra, G., 1988. Basic Methods of Structural Geology. Prentice-Hall.
Martel, S.J., Boger, W.A., 1998. Geometry and mechanics of secondary fracturing around small three-dimensional faults in granitic rock. J. Geophys. Res. 103, 21299–21314.
McGrath, A.G., Davison, I., 1995. Damage zone geometry around fault tips. J. Struct. Geol. 17, 1011–1024.
McNaught, M.A., Mitra, G., 1993. A kinematic model for the origin of footwall synclines. J. Struct. Geol. 15, 805–808.
Mishra, P., Mukhopadhyay, D.K., 2002. Balanced structural models of Mohand and Santaurgarh ramp anticlines, Himalayan foreland fold and thrust belt, Dehradun re- entrant, Uttaranchal. J. Geol. Soc. India 60, 649–661.
Mishra, M., Chakrapani, G.J., 2014. A grain size model for role of tectonics and climate on sedimentation in Siwaliks in Mohand area. J. Geol. Soc. India 84, 105–113.
Mitchell, T.M., Faulkner, D.R., 2009. The nature and origin of off-fault damage surrounding strike-slip fault zones with a wide range of displacements: a field study from the Atacama fault system, northern Chile. J. Struct. Geol. 31, 802–816. http://dx.doi.org/10.1016/j.jsg.2009.05.002.
Mitra, G., Bhattacharyya, K., Mukul, M., 2010. The lesser Himalayan Duplex in Sikkim: implications for variations in himalayan shortening. J. Geol. Soc. India 75, 289–301.
Molnar, P., Tapponnier, P., 1975. Cenozoic tectonics of Asia: effects of a continental collision features of recent continental tectonics in Asia can be interpreted as results of the India- Eurasia collision. Science 189 (4201), 419–426.
Mugnier, J.L., Gajurel, A., Huyghe, P., Jayangondaperumal, R., Jouanne, F., Upreti, B., 2013. Structural interpretation of the great earthquakes of the last millennium in the central Himalaya. Earth Sci. Rev. 127, 30–47. http://dx.doi.org/10.1016/j.earscirev.2013.09.003.
Mukhopadhyay, D.K., Mishra, P., 2004. The Main Frontal Thrust (MFT), northwestern Himalayas: thrust trajectory and hanging wall fold geometry from balanced cross sections. J. Geol. Soc. India 64, 739–746.
Mukul, M., Jaiswal, M., Singhvi, A.K., 2007. Timing of recent out of sequence active deformation in the frontal Himalayan wedge: insights from Darjeeling Sub Himalaya. Geology 35, 999–1002.
Myers, D.J., Nábělek, J.L., Yeats, R.S., 2003. Dislocation modeling of blind thrusts in the eastern Los Angeles basin, California. J. Geophys. Res. 108, 2443. http://dx.doi.org/10.1029/2002JB002150.
Najman, Y., Clift, P., Johnson, M.R.W., Robertson, A.H.F., 1993. Early Stages of Foreland Basin Evolution in the Lesser Himalaya, N India. In: Geological Society, London, Special Publications, vol. 74, pp. 541–558. http://dx.doi.org/10.1144/GSL.SP.1993.074.01.36.
Nakata, T., 1972. Report of Tohoku University, Japan: 7th series (Geography). Geomorphic History and Crustal Movement of the Foothills of the Himalaya, vol. 22, pp. 39–177.
Nakata, T., 1989. Active faults of the Himalaya of India and Nepal. Geol. Soc. Am. Special Pap. 232, 243–264.
Nelson, K.D., Zhao, W., Brown, L.D., Kuo, J., Che, J., Liu, X., Klemperer, S.L., Makovsky, Y., Meissner, R., Mechie, J., Kind, R., Wenzel, F., Ni, J., Nabelek, J., Chen, L., Tan, H., Wei, W., Jones, A.G., Booker, J., Unsworth, M., Kidd, W.S.F., Hauck, M., Alsdorf, D., Ross, A., Cogan, M., Wu, C., Sandvol, E.A., Edwards, M., 1996. Partially molten middle crust beneath southern Tibet: synthesis of project INDEPTH results. Science 274, 1684–1688.
Newman, J., Mitra, G., 1993. Lateral variations in mylonite zone thickness as influenced by fluid-rock interactions, Linville falls fault, North Carolina. J. Struct. Geol. 15 (7), 849–863.
Nicol, A., Gillespie, P.A., Childs, C., Walsh, J.J., 2002. Relay zones between mesoscopic thrust faults in layered sedimentary sequences. J. Struct. Geol. 24, 709–727.
Okada, Y., 1985. Surface deformation due to shear and tensile faults in a half-space. Bull. Seismol. Soc. Am. 75 (4), 1135–1154.
Passchier, C.W., Trouw, R.A.J., 2005. Microtectonics. Springer-Verlag Berlin Heidelberg.
Peacock, D.C.P., Sanderson, D.J., 1991. Displacement and segment linkage and relay ramps in normal fault zones. J. Struct. Geol. 13, 721–733.
Perry, W.J., 1978. Sequential deformation in the central appalachians. Am. J. Sci. 278, 518–542.
Powers, P.M., Lillie, R.J., Yeats, R.S., 1998. Structure and shortening of the Kangra and Dehra Dun reentrants, Sub-Himalaya, India. Geol. Soc. Am. Bull. 110 (8), 1010–1027.
Raiverman, V., Srivastava, A.K., Prasad, D.N., 1994. Structural style in northwestern Himalayan foothills. Himal. Geol. 15, 263–280.
Raiverman, V., Mukerjee, A., Saproo, M.K., Kunte, S.V., Ram, J., 1990. Geological Map of Himalayan Foothills between Yamuna and Sarda Rivers. Institute of Petroleum Exploration, ONCG, Dehra Dun, India.
Rao, A.R., 1993. Magnetic-polarity stratigraphy of upper Siwalik of northwestern Himalayan foothills. Curr. Sci. 64 (11&12), 863–873.
Rao, Y.S.N., Rahman, A.A., Rao, D.P., 1974. On the structure of the Siwalik range between the rivers Yamuna and Ganga. Himal. Geol. 4, 137–150.
Rawling, G.C., Goodwin, L.B., Wilson, J.L., 2001. Internal architecture, permeability structure, and hydrologic significance of contrasting fault-zone types. Geology 29, 43–46.
Sahni, M.R., Khan, E., 1963. Tectonic features of the area around Pinjaur. Curr. Sci. 32 (2), 77–79.
Sangode, S.J., Kumar, R., Ghosh, S.K., 1996. Magnetic polarity stratigraphy of Siwalik sequence of Haripur area (HP), NW Himalaya. J. Geol. Soc. India 47, 683–704.
Sangode, S.J., Kumar, R., Ghosh, S.K., 1999. Paleomagnetic and rock magnetic perspectives on the post-collisional continental sediments of the Himalaya in the Indian sub continent and Gondwana: a paleomagnetic and rock magnetic perspective. In: Radhakrishna, T., Piper, J.D.A. (Eds.), Memoir of the Geological Society of India, vol. 44, pp. 221–248.
Sapkota, S.N., Bollinger, L., Klinger, L., Tapponnier, P., Gaudemer, Y., Tewari, D., 2013. Primary surface ruptures of the great Himalayan earthquakes in 1934 and 1255. Nat. Geosci. 6, 71–76.
Schelling, D., Arita, K., 1991. Thrust tectonics, crustal shortening, and the structure of the far- eastern Nepal Himalaya. Tectonics 10, 851–862.
Scholz, C.H., 1987. Wear and gouge formation in brittle faulting. Geology 15 (6), 493–495.
Seong, Y.B., Kang, H.C., Ree, J.H., Choi, J.H., Lai, Z., Long, H., Yoon, H.O., 2011. Geomorphic constraints on active mountain growth by the lateral propagation of fault- related folding: a case study on Yumu Shan, NE Tibet. J. Asian Earth Sci. 41, 184–194.
Shipton, Z.K., Cowie, P.A., 2003. A conceptual model for the origin of fault damage zone structures in high-porosity sandstone. J. Struct. Geol. 25, 333–344.
Shipton, Z.K., Soden, A.M., Kirkpatrick, J.D., Bright, A.M., Lunn, R.J., 2006. How thick

is a fault? Fault displacement-thickness scaling revisited. In: Abercrombie, R., Mcgarr, A., Di Toro, G., Kanamori, H. (Eds.), Radiated Energy and the Physics of Faulting, American Geophysical Union Monograph Series, vol. 170, pp. 193–198.
Sibson, R.H., 1977. Fault rocks and fault mechanisms. J. Geol. Soc. Lond. 133, 191–213.
Sibson, R.H., 1985. Stopping of earthquake ruptures at dilational fault jogs. Nature 316, 248–251.
Sibson, R.H., 1996. Structural permeability of fluid-driven fault-fracture meshes. J. Struct. Geol. 18, 1031–1042.
Sibson, R.H., 2003. Thickness of the seismic slip zone. Geol. Soc. Am. Bull. 93, 1169–1178.
Singh, A.K., Prakash, B., Mohindra, R., Thomas, J.V., Singhvi, A.K., 2001. Quaternary alluvial fan sedimentation in the Dehradun valley piggy back basin, NW Himalaya: tectonic and paleoclimatic implications. Basin Res. 13, 449–471.
Sinha, R., Sripriyanka, K., Jain, V., Mukul, M., 2014. Avulsion threshold and planform dynamics of the Kosi River in north Bihar (India) and Nepal: a GIS framework. Geomorphology 216, 157–170.
Soliva, R., Schultz, R.A., 2008. Distributed and localized faulting in extensional settings: insights from the North Ethiopian Rift-Afar transition area. Tectonics 27. http://dx.doi.org/10.1029/2007TC002148. TC2003.
Srivastava, P., Mitra, G., 1994. Thrust geometries and deep structure of the outer and lesser Himalaya, Kumaon and Garhwal (India): implication for evolution of the Himalayan fold-and-thrust belt. Tectonics 13, 89–109. http://dx.doi.org/10.1029/93TC01130.
Srivastava, D.C., John, G., 1999. Deformation in the himalayan Frontal Fault zone: evidence f rom small-scale structures in mohand-khara area, NW Himalaya. In: Jain, A.K., Mancikvasagam, R.M. (Eds.), Geodynamics of the NW Himalaya, Gondwana Research Group Memoir, vol. 6, pp. 273–284.
Stein, R.S., Yeats, R.S., 1989. Hidden earthquakes. Sci. Am. 260, 48–57.
Stevens, V.L., Avouac, J.P., 2015. Interseismic coupling on the main Himalayan thrust. Geophys. Res. Lett. 42, 5828–5837. http://dx.doi.org/10.1002/2015GL064845.
Tavani, S., Storti, F., 2011. Layer-parallel shortening templates associated with double-edge fault-propagation folding. In: McClay, K., Shaw, J., Suppe, J. (Eds.), Thrust Fault-related Folding, AAPG Memoir, vol. 94, pp. 121–135.
Thakur, V.C., 1992. Geology of Western Himalaya. Pergamon Press, New York.
Thakur, V.C., 2004. Active tectonics of Himalayan frontal thrust and seismic hazard to Ganga plain. Curr. Sci. 86 (11), 1554–1560.
Thakur, V.C., 2013. Active tectonics of Himalayan Frontal Fault system. Int. J. Earth Sci. (Geol Rundsch) 102, 1791–1810. http://dx.doi.org/10.1007/s00531-013-0891-7.
Thakur, V.C., Pandey, A.K., 2004. Late Quaternary tectonic evolution of Dun in fault bend/propagated fold system, Garhwal Sub-Himalaya. Curr. Sci. 87 (11), 1567–1576.
Thakur, V.C., Pandey, A.K., Suresh, N., 2007. Late Quaternary–Holocene evolution of Dun structure and the himalayan Frontal Fault zone of the garhwal sub-himalaya, NW India. J. Asian Earth Sci. 29 (2–3), 305–319.
Thakur, V.C., Joshi, M., Sahoo, D., Suresh, N., Jayangondapermal, R., Singh, A., 2014. Partitioning of convergence in northwest Sub-Himalaya: estimation of late quaternary uplift and convergence rates across the Kangra reentrant, north India. Int. J. Earth Sci. 103, 1037–1056. http://dx.doi.org/10.1007/s00531-014-1016-7.
Thatcher, W., Bonilla, M.G., 1989. Earthquake Fault Slip Estimation from Geologic, Geodetic and Seismologic Observations: Implications for Earthquake Mechanics and Fault Segmentation. USGS Open-File Report 89-315, pp. 386–399.
Toda, S., Stein, R.S., Richards-Dinger, K., Bozkurt, S., 2005. Forecasting the evolution of seismicity in southern California: animations built on earthquake stress transfer. J. Geophys. Res. 110 (B05S16) http://dx.doi.org/10.1029/2004JB003415.
Torabi, A., Berg, S.S., 2011. Scaling of fault attributes: a review. Mar. Pet. Geol. 28, 1444–1460. http://dx.doi.org/10.1016/j.marpetgeo.2011.04.003.
Valdiya, K.S., 1992. The main boundary thrust zone of the Himalaya, India. Ann. Tect. 6, 54–84 supplement.
Vassallo, R., Mugnier, J.L., Vignon, V., Malik, M.A., Jayangondaperumal, R., Srivastava, P., Carcaillet, J., 2015. Distribution of the late-quaternary deformation in northwestern Himalaya. Earth Planet. Sci. Lett. 411, 241–252.
Vermilye, J.M., Scholz, C.H., 1998. The process zone: a microstructural view of fault growth. J. Geophys. Res. 103, 12223–12237.
Vermilye, J.M., Scholz, C.H., 1999. Fault propagation and segmentation: insight from the microstructural examination of a small fault. J. Struct. Geol. 21, 1623–1636.
Wallace, W.K., Homza, T.X., 2004. Detachment folds versus fault-propagation folds and their truncation by thrust faults. In: McClay, K.R. (Ed.), Thrust Tectonics and Hydrocarbon Systems, AAPG Memoir, vol. 82, pp. 558–578.
Walsh, J.J., Watterson, J., 1988. Analysis of the relationship between the displacements and dimensions of faults. J. Struct. Geol. 10, 239–247.
Walsh, J.J., Nicol, A., Childs, C., 2002. An alternative model for the growth of faults. J. Struct. Geol. 24, 1669–1675.
Watters, T.R., 2004. Elastic dislocation modeling of wrinkle ridges on Mars. Icarus 171, 284–294. http://dx.doi.org/10.1016/j.icarus.2004.05.024.
Watters, T.R., Schultz, R.A., Robinson, M.S., Cook, A.C., 2002. The mechanical and thermal structure of Mercury's early lithosphere. Geophys. Res. Lett. 29, 1–4. http://dx.doi.org/10.1029/2001GL014308.
Wesnousky, S.G., Kumar, S., Mohindra, R., Thakur, V.C., 1999. Uplift and convergence along the himalayan frontal thrust of India. Tectonics 18 (6), 967–976.
Wibberley, C.A.J., Shimamoto, T., 2003. Internal structure and permeability of major strike- slip fault zones: the Median Tectonic Line in Mie Prefecture, southwest Japan. J. Struct. Geol. 25 (1), 59–78.
Wibberley, C.A.J., Yielding, G., Di Toro, G., 2008. Recent Advances in the understanding of fault zone internal structure: a review. In: Wibberley, C.A.J., Kurz, W., Imber, J., Holdsworth, R.E., Coltini, C. (Eds.), The Internal Structure of Fault Zones: Implications for Mechanical and Fluid –Flow Properties, vol. 299. Geological Society of London Special Publication, pp. 5–33.
Yeats, R.S., Lillie, R.J., 1991. Contemporary tectonics of the Himalayan frontal fault system; folds, blind thrusts and the 1905 Kangra earthquake. J. Struct. Geol. 13, 215–225.
Yeats, R.S., Thakur, V.C., 2008. Active faulting south of the Himalayan Front: establishing a new plate boundary. Tectonophysics 453 (1–4), 63–73.
Yeats, R.S., Nakata, T., Farah, A., Fort, M., Mirza, M.A., Pandey, M.R., Stein, R.S., 1992. The Himalayan frontal fault system. In: Bucknam, R.C., Hancock, P.L. (Eds.), Major Active Faults of the World: Results of IGCP Project 206. Annales Tectonicae (Supp. to Vol. VI), pp. 85–98.
Yin, A., 2006. Cenozoic tectonic evolution of the Himalayan orogen as constrained by along strike variation of structural geometry, exhumation history, and foreland sedimentation. Earth Sci. Rev. 76, 1–131.
Zhao, W., Nelson, K.D., Project INDEPTH Team, 1993. Deep seismic reflection evidence for continental underthrusting beneath southern Tibet. Nature 366, 557–559.